An efficient modeling framework for wall heat flux prediction in rocket combustion chambers using non adiabatic flamelets and wall-functions

4 authors:

Giuseppe Indelicato
Sapienza University of Rome
10 PUBLICATIONS   **52** CITATIONS

SEE PROFILE

Pasquale Eduardo Lapenna
Sapienza University of Rome
41 PUBLICATIONS   **317** CITATIONS

SEE PROFILE

Arianna Remiddi
Sapienza University of Rome
5 PUBLICATIONS   **7** CITATIONS

SEE PROFILE

Francesco Creta
Sapienza University of Rome
76 PUBLICATIONS   **1,152** CITATIONS

SEE PROFILE

Some of the authors of this publication are also working on these related projects:

Project   Automatic procedures for the simplification of chemical kinetic mechanisms based on CSP View project

Project   Supercritical fluid mixing and combustion View project

An efficient modeling framework for wall heat flux prediction in rocket combustion chambers using non adiabatic flamelets and wall-functions

G. Indelicato[a], P. E. Lapenna[a], A. Remiddi[a], F. Creta[a]

[a]*Department of Mechanical and Aerospace Engineering, Sapienza University of Rome, Italy.*

Abstract

In this work an efficient numerical framework for the prediction of wall heat loads in Liquid Rocket Engine combustion chambers is presented. The proposed framework is based on a new version of the non-adiabatic flamelet model and on wall functions for turbulent boundary layer modeling. Different wall function models are applied to 2D and 3D wall heat flux simulations of an experimental single-element gaseous oxygen-gaseous methane combustor in an Unsteady Reynolds Averaged Navier Stokes context. A systematic analysis and a comprehensive comparison of the selected wall models is carried out. The role of the constant or variable properties assumption on the near-wall turbulent quantities affecting the wall heat flux is assessed and the resulting friction velocity scaling investigated. When the skin friction velocity based on the local turbulent kinetic energy is defined by considering constant properties across the boundary layer, the equilibrium boundary layer assumption is not fulfilled and a significant overestimation of the wall

*corresponding author: Giuseppe Indelicato
Email address: `giuseppe.indelicato@uniroma1.it` ()

heat flux is observed. Results obtained with the corrected near-wall turbulence modeling, on the other hand, showed a substantial improvement in terms of wall heat flux when compared with both experimental data and higher fidelity simulations results.

Keywords: Liquid Rocket Engine, Turbulent combustion, Wall heat flux, Non-adiabatic flamelets, Wall functions

---

Nomenclature

Symbols

$\cdot''$ Fluctuating component from Favre decomposition

$\Delta\cdot, \Delta$ Distance of a point from the wall, cell width

δ Kronecker delta funtion

κ Von Karman constant

$\bar{\cdot}$ Reynolds averaging operator

∂ Partial derivative

$\partial/\partial y$ Wall normal derivative

σ_k Model constant

$\tilde{\cdot}$ Favre averaging operator

C Model constant

C_d Model constant

C_g Model constant

C_χ Model constant

C_μ Model constant

d Total differential

E Wall roughness constant

n_s Number of species

$p(\cdot)$ Probability density function

R Gas constant

Quantities

α Thermal diffusivity $(kg/m/s)$

χ Scalar dissipation rate (s^{-1})

$\dot{\omega}$ Species source term $(kg/m^3/s)$

$\dot{\omega}_T$ Energy source term $(J/m^3/s)$

ϵ Turbulent dissipation rate (m^2/s^3)

λ Thermal conductivity $(W/m/K)$

μ Dynamic viscosity $(kg/m/s)$

ν Kinematic viscosity (m^2/s)

ϕ Enthalpy defect (J/kg)

ρ Density (kg/m^3)

τ Shear stress $(kg/m/s^2)$

$\mathbf{u}$ Velocity vector (m/s)

$\mathbf{x}$ Cartesian coordinate vector (m)

C_p Specific heat at constant pressure $(J/kg/K)$

h Specific enthalpy (J/kg)

k Turbulent kinetic energy (m^2/s^2)

Le Lewis number

p Pressure (Pa)

P_k Turbulent kinetic energy production (m^2/s^3)

Pr Prandtl number

q Heat flux $(J/m^2/s)$

Sc Schmidt number

T Temperature (K)

t Time (s)

T_τ Skin friction temperature (K)

u_τ Skin friction velocity (m/s)

Y Mass fraction

Z Mixture fraction

Z''^2 Mixture fraction variance

Sub- and Superscripts

$+$ Non-dimensional wall value

ad Adiabatic value

F Fuel-side value

i, j Cartesian coordinate indexes

k Species index

Ox Oxidizer-side value

P Value at the last cell centre before the wall

st Stoichiometric value

t Turbulent value

w Wall value

1. Introduction

High pressure combustion in Liquid Rocket Engines (LRE) has regained attention in recent years given the efforts of private and public international space agencies in the development of resusable and efficient methane-fueled

engines [1, 2, 3, 4], given the attractive properties of methane as a possible cheaper and denser replacement for hydrogen in launch vehicles [5, 6]. The extreme operative conditions under which these devices work and the interplay of different phenomena, however, make its experimental investigation prohibitive and economically expensive. In this context Computational Fluid Dynamics (CFD) provides a fundamental support in the investigation of high pressure, turbulent and reactive flows. The development of heat transfer, turbulence and progressively more complex physical models, have indeed broadened the base of CFD applications and determined its widespread use by both industrial and scientific communities [7]. Nowadays, therefore, the challenge is focused on the development of efficient and cost-saving numerical tools able to provide an active support in the design process of these engines and their components. Particular attention is devoted to the prediction of thermo-mechanical stresses inside the engines, in order to reduce the risk of failure during operative conditions and increase their life-time. For this purpose it is fundamental to estimate the gas-to-wall heat transfer. High Performance Computing (HPC) resources, in this context, have promoted the development of highly resolved high fidelity simulations. The resolution criteria required by simulations of wall-bounded flows, however, while particularly interesting for heat transfer investigations, still represent a bottle-neck and necessitate the use of wall models or wall functions as approximate wall boundary conditions [8, 9].

Wall functions are indeed conceived to model a turbulent boundary layer and mitigate the computational cost associated to the near-wall flow resolution. Their development has been largely based on the pioneering work

6

of Launder and Spalding [10] and on the well-known equilibrium boundary layer assumption, which assumes a constant shear stress across the boundary layer by neglecting unsteady, pressure gradient and convective terms in the momentum equation written in the thin boundary layer assumption. Such hypothesis is grounded on the statistical interpretation that the considered near-wall resolution contains an almost infinite number of eddies and that the time step used for the integration is much larger than the timescale of these near-wall eddies. According to Piomelli [9] this assumption generally holds as long as we consider simple geometries and extremely high Reynolds numbers; conversely, it needs to be revisited in the presence of strong favorable or adverse pressure gradients, in separated flows or in highly three-dimensional flows. Based on this, wall functions were proposed to match the wall shear stress on relatively coarse near-wall resolutions, given the underlying underestimation of the wall-normal velocity gradient caused by the first off-grid node lying in the outer flow region. The previously mentioned equilibrium assumption indeed results in the existence of a logarithmic velocity profile that can be used to relate the velocity in the outer layer to the wall stress [9]. An effective viscosity can then be defined to compensate the unresolved velocity gradient and match the estimated wall shear stress.

As a first attempt to calculate the wall heat transfer in a wall modeled context, it is possible to extend the previously described procedure by scaling the effective viscosity with a constant turbulent Prandtl number Pr_t in order to obtain an effective thermal diffusivity and predict a value of wall heat flux. This is also known as the Reynolds analogy, which assumes the kinematic and the thermal boundary layer to be identical, apart from a proportional-

ity factor, and the near-wall thermal field to be isotropic [11]. The validity of this assumption has been mostly tested on fully developed channel flow configurations for incompressible flows [12] and effectively showed a constant value of $0.7 - 0.85$ attained by the Pr_t in the outer flow. More recently Cabrit and Nicoud [13] showed that the proposed value 0.7 holds even in the case of non-neglegible chemical and compressibility effects in the turbulent boundary layer. The mentioned Reynolds analogy provides for a relatively simple prediction of the wall heat flux, but at the same time shows a lack of physical modeling of the thermal field. Therefore, more specific wall functions for the determination of the wall heat flux were obtained starting from the integration of the energy equation across the boundary layer. These models are generally referred to as thermal wall functions and fall in the category of analyitical wall models. Their common characteristic is to provide a modeled value of wall heat flux based on the outer flow conditions. In this category, we recall Kays and Crawford [14], who obtained an algebraic closed-form solution of the mentioned equation limited to air. Angelberger [15] and Han and Reitz [16] separately obtained similar expressions for the wall heat flux, by considering variable properties across the boundary layer in contrast to Kays and Crawford. A detailed description of the derivation of these models can be found in the cited articles and in Berni et al. [17] while a comprehensive comparison of their performances in an Internal Combustion (IC) engine is found in Rakopoulos et al. [18]. The mentioned models rely on the common assumptions of frozen composition in the boundary layer, neglegible pressure gradients, quasi-steady flow and neglegible radiation and viscous dissipation. Different formulations then arise according to the inclusion of

non-equilibrium effects such as pressure work term [19], unsteadiness [20, 21] and convective term [21].

In the context of rocket engines, Nichols and Nelson [22] formulated a coupled velocity-temperature wall function based on theoretical near-wall profiles proposed by White [23]. The proposed wall function was tested on a flat plate configuration, with and without heat transfer, and on an experimental, cooled, non-reacting convergent-divergent nozzle with heated air developed at Jet Propulsion Laboratory (JPL) in 1963 by Back, Massier and Gier [24]. The effect of different grid spacings was assessed and results showed a good agreement with the theory and the available experimental data. Similarly Fico et al. [25] led a comparative study on the previously cited experimental configuration by using different wall function formulations. They also carried out a validation campaign on a reactive nozzle test case based on the combustion of gaseous oxygen (GOx) and gaseous hydrogen (GH2) at 5.2 MPa. Cabrit and Nicoud [13] proposed a coupled-model for the determination of the wall shear stress and the wall heat flux in a wall modeled framework, starting from a Direct Numerical Simulation (DNS) campaign of reacting and non-reacting turbulent channel flows. The performance of the model was assessed in an a-priori fashion and provided a good reproduction of the resolved wall heat flux and wall shear stress. More recently Muto et al. [26] developed a wall model for reacting turbulent flows for predicting heat transfer in rocket engine combustion chambers, with the inclusion of chemical reactions and variable property effects modeled with an equilibrium chemistry tabulated approach. The proposed equilibrium wall model was validated in two hydrogen/oxygen reacting cases, namely a reacting turbulent channel flow and

9

a rocket combustion chamber, providing comparatively improved prediction capabilities over other wall models. In the context of methane-fueled LRE combustion chambers, a large number of experimental [27, 28, 29] and numerical [30, 31, 32, 33, 34, 35, 36] investigations have been performed in recent years. Numerical simulations based on non-adiabatic tabulated approaches (such as the flamelet model [37]) and wall functions for wall heat flux predictions, in particular, showed good results compared to the available experimental data, although a large scatter of the calculated wall heat flux was observed depending on the employed numerical setting. Moreover, despite efforts in investigating the effect of the frozen or equilibrium chemistry assumption on the ensuing wall heat flux [38, 39, 40] and of different turbulence [30, 41] and turbulence-chemistry interaction [32] models, to the best of the authors' knowledge, a systematic analysis of wall function models as well as their interaction with flamelet-based turbulent combustion approaches for the simulation of realistic methane-fueled LRE combustion chambers is still missing.

In this context, this work presents an efficient numerical framework for the simulation of high-pressure turbulent flows in LRE combustion chambers and the prediction of wall heat loads. Different wall function models taken from the literature are implemented in a flamelet-based finite volume solver and applied to the evaluation of wall heat flux in LRE-like conditions. A new non-adiabatic flamelet model is proposed retaining non-adiabatic effects for the evaluation of thermal loads. The proposed framework is tested by means of 2D and 3D unsteady Reynolds Averaged Navier Stokes (URANS) simulations of an experimental single-element gaseous oxygen-gaseous methane

10

(GOx/GCH4) combustor, for which a comparison among the selected wall functions is carried out.

The work is organized as follows: Section 2 describes the newly developed non-adiabatic flamelet model. Section 3 presents the governing equations and how the wall heat flux is modeled in a wall-modeled context. Section 4 describes the wall function models employed in the present work and discusses their implementation in a flamelet-based framework; the effect of the variable or constant properties assumption across the boundary layer on the near-wall turbulent quantities is also assessed, given their impact on the selected models. Section 5 presents the test case chosen for the validation of the proposed numerical framework and results of the 2D and 3D URANS wall modeled simulations of the selected test case: differences between the wall heat fluxes obtained with the tested models are presented and discussed. In addition a comparison with results obtained from higher fidelity simulations on the same chamber taken from the literature is reported. Conclusive remarks of the work are reported in Section 6.

2. Non-adiabatic flamelet model

The combustion model is based on the steady flamelet approach [37], wherein a turbulent flame is regarded in the high Damköhler limit as an ensemble of thin laminar flames, namely flamelets. Flame structures can be obtained by solving the flamelet equations in the mixture fraction space Z, reported below in their unsteady form:

11

$$\frac{\partial Y_k}{\partial t} = \frac{1}{2}\chi\frac{\partial^2 Y_k}{\partial Z^2} + \frac{\dot{\omega}_k}{\rho} \tag{1}$$

$$\frac{\partial T}{\partial t} = \frac{1}{2}\chi\frac{1}{C_p}\Big[\frac{\partial^2 h}{\partial Z^2} + \sum_{k=1}^{n_s} h_k \frac{\partial^2 Y_k}{\partial Z^2}\Big] + \frac{\dot{\omega}_T}{C_p\rho} \tag{2}$$

where t is time, Y_k the mass fraction of the $k-$th species of the mixture, T the temperature, ρ the density, χ the scalar dissipation rate, $\dot{\omega}_k$ and $\dot{\omega}_T$ the k-th species and heat production rates respectively, C_p the specific heat at constant pressure and h the enthalpy of the mixture defined as $h = \sum_{k=1}^{n_s} Y_k h_k = \sum_{k=1}^{n_s} Y_k h_{s,k} + \sum_{k=1}^{n_s} Y_k \Delta h_{f,k}^0$, where $h_{s,k}$ and $\Delta h_{f,k}^0$ are the sensible enthalpy and the heat of formation of the k-th species, respectively. The basic flamelet manifold, hence the steady state solutions of Eqs. (1)-(2), can be extended to include non-adiabatic effects, when an additional variable ϕ, representing the enthalpy defect is introduced. In the formulation of Marracino and Lentini [42], a uniform enthalphy defect is applied throughout the mixture fraction space. This however was observed [43, 44] to result in unphysical temperature values, especially near the fuel and oxidizer boundaries. To avoid this issue, we introduce here a new non-adiabatic formulation wherein a functional dependence modulating the enthalpy loss is envisaged. The main conjecture is to localize the maximum enthalphy loss at the stoichiometric mixture fraction, Z_{st}, while no loss is assumed at $Z = 0$ and $Z = 1$. This approach is indeed similar to the one used by Kim et al. [45] where the enthalpy substraction in the mixture fraction space is conversely modeled as a bell-shape profile. Lee et al. [46] on the other hand introduced a source term in the unsteady flamelet equations in order to take into account non-adiabatic effects, modeled as a convective heat-loss process evolving on

12

a time scale based on a Nusselt-number relation. Similarly, Wollny et al. [47] tested two approaches: a heat release damping (HRD) method, decreasing the chemical source term in the flamelet energy equation by a constant factor, and an artificial radiation (AR) approach providing an augmented temperature dependent radiative source term. Differently Ma et al. [48] introduced a permeable thermal boundary condition in the solution of a counter flow diffusion flame configuration, in order to retain wall-induced non-adiabatic effects on the ensuing flamelet structures.

In the present work the function $f(Z, Z_{st})$ modulating the defect, albeit reasonable, is rather arbitrary and should be validated by means of a not as yet available, paradigmatic DNS study of a diffusive flame impinging on a non adiabatic wall, which would reveal the distribution of enthalpy across the mixture fraction space. We choose function $f(Z, Z_{st})$ as a piecewise linear function (see Eq. (3)), representing the easiest logical improvement with respect to the uniform defect [42] which avoids the unphysical temperature values.

$$f(Z, Z_{st}) = \begin{cases} \frac{Z}{Z_{st}} & Z \leq Z_{st} \\ 1 - \frac{Z - Z_{st}}{1 - Z_{st}} & Z > Z_{st} \end{cases} \tag{3}$$

The generic thermodynamic property Ψ (such as density, temperature or species mass fraction) is therefore obtained as $\Psi(Z, \chi_{st}, \phi)$, being χ_{st} the stoichiometric scalar dissipation rate. Non-adiabatic effects in particular are retained with two tabulation techinques, namely the frozen (F) and the fully non-adiabatic (NA) approach. In the NA framework, both the temperature and species mass fractions are subject to non-adiabatic effects. The underlying assumption is that the flame instantaneously adapts to non-adiabatic
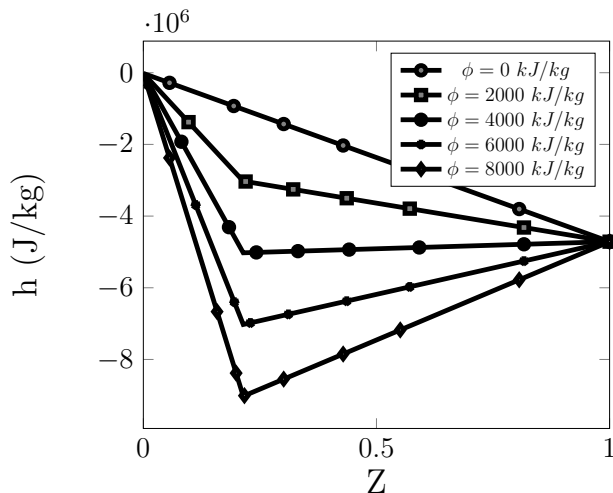
13

Figure 1: Non-adiabatic enthalpy profiles obtained with the new flamelet model for increasing values of the defect ϕ.

phenomena, as those occurring when the flame approaches an isothermal wall. Non-adiabatic flamelets obtained with the NA model are computed by solving Eq. (1) for species mass fractions and imposing, for each user-prescribed ϕ, a steady state enthalpy profile $h(Z)$ in the form

$$h(Z, \phi) = h_{ad}(Z) - \phi \cdot f(Z, Z_{st}) \qquad (4)$$

In Eq. (4) $h_{ad}(Z)$ is the adiabatic enthalpy of the mixture, which at steady state is a linear function of Z [45]

$$h_{ad}(Z) = h_{Ox} + Z(h_F - h_{Ox}) \qquad (5)$$

being h_{Ox} and h_F the static enthalpies of oxidizer and fuel, respectively. Figure 1 reports Eq. (4) plotted for different values of the defect ϕ. In the

14

semi-adiabatic or frozen (F) approach, on the other hand, only the temperature is subjected to non-adiabatic effects, while the mixture composition is frozen and kept equal to the adiabatic one. In contrast with the previous assumption for the NA model, here it is assumed that the composition evolves on an infinite time scale in order to adapt to non-adiabatic effects. The physical underlying assumption is that reaction rates become vanishingly small as the flame perceives non-adiabatic effects, thus preventing further reactions such as recombinations close to the wall. An example of flame structures generated with the NA and the F model is given in Fig. 2. The flamelets are solved with the OpenSMOKE++ [49] library developed by the CRECK modeling group and modified in-house in order to deal with flows under rocket-relevant conditions [50]. The employed chemical mechanism is the GRI 3.0 [51] for an oxygen-methane mixture, which although developed for atmospheric pressures has already found application in previous studies of high pressure methane oxy-combustion in rocket-like configurations [52, 44, 53, 54, 50]. The chosen thermodynamic conditions (pressure $p = 20$ bar, oxidizer inlet temperature $T_{Ox} = 278$ K, fuel inlet temperature $T_F = 269$ K and $Z_{st} = 0.2$) refer to the experimental configuration which will be simulated in the following sections.

As can be observed from Fig. 2, as the enthalpy of the mixture is lowered, the effect of recombination reactions leads to the depletion of radicals (mostly OH and CO) in favor of H_2O and CO_2. The exothermicity of such processes leads to relatively high temperatures even in the presence of considerable heat losses, explaining the differences in the temperature profiles between the NA and the F approach for a given enthalpy defect reported in Fig. 2
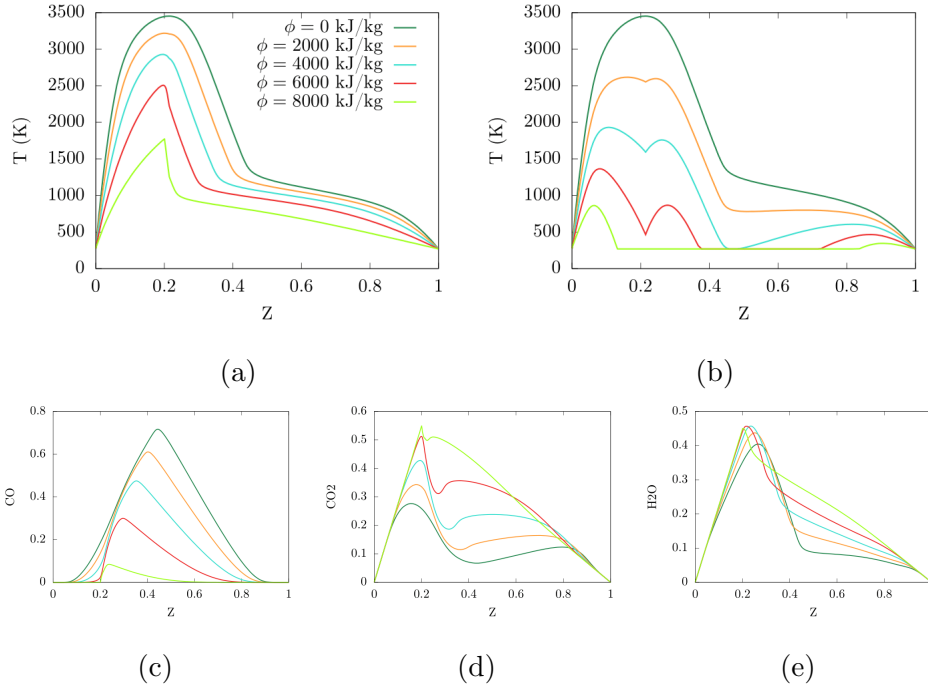
Figure 2: Top: temperature profiles obtained at different values of the enthalpy defect ϕ and $\chi = 0$ s^{-1} for the NA (a) and the F (b) model. Bottom: mass fraction profiles obtained with the NA model for selected species at the same degrees of defect: CO (c), CO_2 (d) and H_2O (e).

(a)-(b). From the total differential of enthalpy under ideal gas conditions

$$dh = C_p dT + \sum_k h_k dY_k \tag{6}$$

we can see that for a given enthalpy defect, the F approach, for which $dY_k = 0$ by definition, fully translates the dh to a change in temperature, while the NA approach redistributes the defect among the two terms in the right-hand-side of Eq. (6), thus causing a lower dT.

Turbulence-chemistry interaction is taken into account by means of a presumed Probability Density Function (PDF) approach in which the laminar thermodynamic quantities are convoluted with a multi-variate PDF in the form

$$\widetilde{\Psi} = \int \Psi(Z, \chi_{st}, \phi) p(Z, \chi_{st}, \phi) dZ d\chi_{st} d\phi \tag{7}$$

in order to obtain mean quantities $\widetilde{\Psi}$ which are then extracted from the flamelet libraries at run time according to some entry values

$$\widetilde{\Psi} = \widetilde{\Psi}(\widetilde{Z}, \widetilde{Z''^2}, \widetilde{\chi}_{st}, \widetilde{\phi}). \tag{8}$$

In Eqs. (7) and (8), the symbol $\widetilde{\star} = \overline{\rho\star}/\bar{\rho}$ represents the Favre averaging operator while $\bar{\star}$ denotes a Reynolds mean quantity; $\widetilde{Z''^2}$ is the mixture fraction variance used to model the unresolved fluctuations of Z. The PDF in Eq. (7) is commonly modeled according to statistical independence assumptions, as the product of single-variate PDFs. In particular a β-PDF is generally assumed for the mixture fraction [55, 56, 50, 57, 58] and a log-normal or a Dirac delta for the scalar dissipation. In the present work a Dirac delta distribution is assumed for both the scalar dissipation and the enthalpy defect, similarly to [46].

17

3. Governing equations

Equation (8) highlights the entry values needed by the CFD code for the look-up process of the flamelet libraries. Transport equations for the mixture fraction and its variance, reading

$$\frac{\partial(\bar{\rho}\widetilde{Z})}{\partial t} + \frac{\partial(\bar{\rho}\widetilde{\mathbf{u}}_i\widetilde{Z})}{\partial \mathbf{x}_i} = \frac{\partial}{\partial \mathbf{x}_i}\left[\left(\bar{\alpha} + \frac{\bar{\rho}\nu_t}{Sc_t}\right)\frac{\partial\widetilde{Z}}{\partial \mathbf{x}_i}\right] \tag{9}$$

$$\frac{\partial(\bar{\rho}\widetilde{Z''^2})}{\partial t} + \frac{\partial(\bar{\rho}\widetilde{\mathbf{u}}_i\widetilde{Z''^2})}{\partial \mathbf{x}_i} = \frac{\partial}{\partial \mathbf{x}_i}\left[\left(\bar{\alpha} + \frac{\bar{\rho}\nu_t}{Sc_t}\right)\frac{\partial\widetilde{Z''^2}}{\partial \mathbf{x}_i}\right] +$$

$$+C_g\left(\bar{\alpha} + \frac{\bar{\rho}\nu_t}{Sc_t}\right)\left|\frac{\partial\widetilde{Z}}{\partial \mathbf{x}_i}\right|^2 - C_d\bar{\rho}\frac{\epsilon}{k}\cdot\widetilde{Z''^2} \tag{10}$$

are solved at run time to extract mean temperature, mass fractions and thermodynamic properties from the flamelet libraries, together with the entry values for the stoichiometric scalar dissipation $\widetilde{\chi}_{st}$, given by

$$\widetilde{\chi}_{st} = C_\chi\frac{\epsilon}{k}\widetilde{Z''^2} \tag{11}$$

where $C_\chi = 2.00$. In the above equations $\mathbf{u}_i$ is the $i-$th component of the velocity vector in the cartesian coordinate $\mathbf{x}_i$ $(i = 1, 2, 3)$, α the laminar thermal diffusivity, C_g and C_d model constants respectively set to 2.86 and 2.00, Sc_t a turbulent Schmidt number equal to the turbulent Prandtl number $Pr_t = 0.85$; k and ϵ are the turbulent kinetic energy and its dissipation rate, given by the standard $k - \epsilon$ and used to model the turbulent viscosity ν_t, appearing in Eq. (10) and (9), as

$$\nu_t = C_\mu\frac{k^2}{\epsilon} \tag{12}$$

18

with $C_\mu = 0.09$, and in the conservation of momentum

$$\frac{\partial(\bar{\rho}\widetilde{\mathbf{u}}_i)}{\partial t} + \frac{\partial(\bar{\rho}\widetilde{\mathbf{u}}_i\widetilde{u}_j)}{\partial x_j} = -\frac{\partial \bar{p}}{\partial \mathbf{x}_i} + \frac{\partial}{\partial x_j}\left[(\bar{\mu} + \bar{\rho}\nu_t)\left(\frac{\partial\widetilde{\mathbf{u}}_i}{\partial x_j} + \frac{\partial\widetilde{u}_j}{\partial \mathbf{x}_i} - \frac{2}{3}\delta_{ij}\frac{\partial\widetilde{u}_l}{\partial x_l}\right)\right]$$
(13)

where μ is the dynamic viscosity of the mixture and δ_{ij} the Kronecker delta. A transport equation for the enthalpy of the mixture is also solved, reading

$$\frac{\partial(\bar{\rho}\widetilde{h})}{\partial t} + \frac{\partial(\bar{\rho}\widetilde{\mathbf{u}}_i\widetilde{h})}{\partial \mathbf{x}_i} = \frac{\partial \bar{q}_i}{\partial \mathbf{x}_i}$$
(14)

where $\bar{q}_i$ is the average energy flux. In the right-hand-side of Eq. (14) the material derivative of pressure and the viscous dissipation terms are neglected according to the low-Mach number assumption.

Under the hypothesis of negligible viscous dissipation, no Soret nor Dufour effects and no radiation heat transfer phenomena, the laminar energy flux q_i reduces to the Fourier term plus a contribution coming from the enthalpy flux due to species molecular diffusion [13]

$$q_i = -\lambda\frac{\partial T}{\partial \mathbf{x}_i} - \frac{\mu}{Sc}\sum_{k=1}^{n_s}h_k\frac{\partial Y_k}{\partial \mathbf{x}_i}$$
(15)

where λ is the thermal conductivity of the mixture, while the Fick's law together with a constant molecular Schmidt number Sc assumption were used to model the mass flux. By expressing Eq. (15) in terms of enthalpy gradient under ideal gas hypothesis $(\frac{\partial h}{\partial p}|_{T,Y_k} = 0)$, we have

$$\frac{\partial T}{\partial \mathbf{x}_i} = \frac{1}{C_p}\left(\frac{\partial h}{\partial \mathbf{x}_i} - \sum_{k=1}^{n_s}h_k\frac{\partial Y_k}{\partial \mathbf{x}_i}\right)$$
(16)

19

which substituted into Eq. (15) gives

$$q_i = -\frac{\lambda}{C_p}\frac{\partial h}{\partial \mathbf{x}_i} + \left(\frac{\lambda}{C_p} - \frac{\mu}{Sc}\right)\sum_{k=1}^{n_s} h_k\frac{\partial Y_k}{\partial \mathbf{x}_i}. \qquad (17)$$

Under the assumption of unitary Lewis number ($Le = Sc/Pr = 1$, being Pr the molecular Prandtl number) the second term in the right-hand-side of the above equation vanishes being $\alpha = \lambda/C_p = \mu/Pr$ and the following identity holds by comparing Eq. (17) and Eq. (15)

$$q_i = -\alpha\frac{\partial h}{\partial \mathbf{x}_i} = -\lambda\frac{\partial T}{\partial \mathbf{x}_i} - \frac{\mu}{Sc}\sum_{k=1}^{n_s} h_k\frac{\partial Y_k}{\partial \mathbf{x}_i} \qquad (18)$$

It is worth mentioning that at the wall only the Fourier contribution in the right-hand-side of Eq. (18) remains, being $\frac{\partial \widetilde{Y_k}}{\partial y} = 0$ for a generic non-reacting surface and y the wall normal coordinate. When an equilibrium tabulation technique is employed, however, non-physical gradients of species are observed at the wall, as also shown from DNS analysis [13]. The wall heat flux calculated with the enthalpy gradient-based expression of Eq. (18), therefore, would not coincide with the Fourier term alone but would rather result in an overestimation. In this context the frozen assumption can be considered a more realistic modelization of the near-wall flow field. When dealing with turbulent flows, the averaging procedure of the energy equation gives rise to a turbulent enthalpy flux which can be modeled by means of a classical gradient assumption, leading to the introduction of a turbulent thermal diffusivity α_t. In the internal field the latter is derived from the turbulent viscosity of Eq. (12) by setting a value for the turbulent Prandtl number Pr_t. A final expression for the average energy flux $\bar{q}_i$ is then given

by

$$\bar{q}_i = -\left(\bar{\alpha} + \alpha_t\right)\frac{\partial \widetilde{h}}{\partial \mathbf{x}_i} \tag{19}$$

When evaluated at the wall, Eq. (19) clearly shows the main contributions in the determination of the wall heat flux: (i) the chosen chemistry model (frozen or non-adiabatic) which enters in Eq. (19) both in the evaluation of the laminar thermal diffusivity at the wall and in the magnitude of the wall normal enthalpy gradient due to the neglected heat released by recombinations; (ii) a model for the turbulent wall thermal diffusivity $\alpha_{t,w}$. As mentioned in the introduction, different works focused on the investigation of point (i), such as [38, 39, 40], while our focus is mainly on point (ii). Consequently, wall modeled simulations will be carried out employing the frozen chemistry model previousy described. This choice is also driven by the previous observations on the non-physical wall enthalpy gradients ensuing when the equilibrium approach is used and by the consistency with the frozen composition assumption usually adopted in the derivation of the thermal wall functions which will be used in the mentioned simulations. The next section therefore describes the different wall functions used to model the turbulent wall thermal diffusivity.

4. Wall modeling

In order to save computational resources in view of 3D simulations on complex geometries, wall functions are introduced for turbulent boundary layer modeling. The latter generally prescribe algebraic boundary conditions for mean turbulent quantities based on flow quantities far from the wall [13, 25]. According to the standard wall function approach (Launder and

21

Spalding [10]) the last computational node before the wall should fall within the outer layer of a turbulent boundary layer, in order to patch the outer flow solution with the universal velocity and temperature profiles [59, 10, 12]. Near wall velocity profiles are indeed shown to collapse onto a single curve when non-dimensionalized based on the skin friction velocity u_τ. The latter is defined as $\sqrt{|\tau_w|/\rho_w}$ [60], being τ_w the longitudinal wall shear stress. Non-dimensional quantities, referred to with the superscritp $+$, are then defined as $y^+ = \Delta y_P u_\tau / \nu_w$, $u^+ = \widetilde{u}/u_\tau$, $T^+ = (T_w - \widetilde{T})/T_\tau$, $k^+ = k/u_\tau^2$, $\epsilon^+ = \epsilon \nu_w / u_\tau^4$ and $\nu^+ = \nu_t / \nu_w$, where $T_\tau = q_w/(\rho_w C_{p,w} u_\tau)$ is the skin friction temperature while Δy_P is the distance between the last grid node before the wall, denoted by the subscript P, and the wall, denoted by the subscript w. In order to avoid singularities in the definition of u_τ, caused by wall shear stress vanishing at re-attachment and separating points [61], Launder and Spalding [62] proposed the use of the local turbulent kinetic energy, k_P, as a characteristic turbulent velocity scale. Based on this assumption the skin friction velocity is usually retrieved as [63, 25]

$$u_\tau = C_\mu^{1/4} \sqrt{k_P} \tag{20}$$

Different authors [60, 64], however, pointed out that the standard scaling may fail in case of strong thermal gradients in proximity of the wall, such as those induced by the considerable wall heat losses experienced in rocket combustion chambers, whenever compressibility effects in the boundary layer were neglected.

In the following we discuss some of the existing wall function models for the prediction of the wall heat flux, regrouped in three categories, namely A, B and C, according to the progressively higher degree of complexity.

22

4.1. Wall functions based on Reynolds analogy (group A)

The definition of this class of wall functions is inspired by Bredberg [11] and regroups all the models which assume a similarity between the kinematic and the thermal boundary layer. They generally employ assumptions of constant properties and single component flow across the boundary layer. A turbulent thermal diffusivity at the wall is therefore obtained by scaling the wall turbulent viscosity with a prescribed value of the turbulent Prandtl number Pr_t, as

$$\alpha_{t,w} = \frac{\bar{\rho}_w \nu_{t,w}}{Pr_t}. \tag{21}$$

The Pr_t is set to 1 in order to retrieve the classical Reynolds assumption although empirical relations based on experimental and numerical results showed that a more realistic value of 0.85 is expected [12]. This value is used in the present work together with the following law for the wall turbulent viscosity

$$\nu_{t,w} = \nu_w \left(\frac{\kappa y^+}{\ln(Ey^+)} - 1 \right) \tag{22}$$

being $\kappa = 0.41$ and $E = 9.8$. The above is derived from compensating the unresolved wall shear stress in a wall-modeled context via the introduction of a turbulent viscosity. Its derivation, which can be found in [65], is based on the existence of the standard law of the wall for the velocity, thus addressing this model to a standard wall function approach [11].

4.2. Thermal wall functions (group B)

This class of wall functions accounts for the variation of properties across the boundary layer (mainly density and viscosity [15, 16]) due to strong temperature gradients. The latter are thus often referred to as compressible

wall function formulations [18]. They generally originate from the integration of the energy transport equation in the boundary layer, written under the following main assumptions [16, 66]:

- Wall normal gradients much greater than those parallel to the wall
- Neglegible pressure gradients, thus pressure only a function of time
- No Dufour or Soret effects nor radiation phenomena in the energy flux
- Ideal gas assumption and constant C_p across the boundary layer

Different formulations then arise according to the inclusion of differential diffusion effects [26], viscous dissipation [26] or pressure work [67] terms. In the present work the thermal wall function formulation developed by Han and Reitz [16] is chosen as representative of this category. This model accounts for the experimental increase of the Pr_t in the viscous sub-layer [12] by means of a polynomial fitting of ν^+/Pr_t according to a number of empirical laws [68]. The derivation of the model originates from the following non-dimensional form of the energy equation, valid under the previously introduced assumptions

$$\frac{\rho C_p u_\tau dT}{q_w} = \frac{1}{\left(\frac{1}{Pr} + \frac{\nu^+}{Pr_t}\right)} dy^+ + \frac{G^+ y^+}{\left(\frac{1}{Pr} + \frac{\nu^+}{Pr_t}\right)} dy^+ \tag{23}$$

where G^+ is a non-dimensional average chemical heat release. The left-hand-side of Eq. (23) can be integrated between the wall and the grid node P to define a T^+ as

$$T^+ = \int_{T_w}^{T} \frac{\rho C_p u_\tau}{q_w} dT = \frac{\rho C_p u_\tau T \ln(T/T_w)}{q_w} \tag{24}$$

where the last identity is obtained by multiplying and dividing by T and recasting $\rho C_p T = p C_p / R$ using the ideal gas law, being R the gas constant.

24

This quantity is then brought outside of the integral according to the previous assumptions. This step is generally valid for single-component and ideal gas flows. When dealing with an ideal gas mixture, as in the present case, the quantity p/R can still be assumed constant in the boundary layer as long as we consider frozen composition; the C_p, however, is still a function of temperature. Therefore in the present work a mean term $\overline{C_p}$ is considered for the specific heat in order to write the last identity in Eq. (24). The proposed modelization consists in a simple arithmetic average betweem the value at the last node and the wall, as inspired by Ikegami et al. [69]. The analytical integration of the right-hand-side of Eq. (23) is made by employing the cited polynomial fitting for ν^+/Pr_t, which finally leads to

$$T^+ = 2.1 \ln(y^+) + 2.1 G^+ y^+ + 33.4 G^+ + 2.5 \tag{25}$$

If the chemical heat release is neglected, and thus a frozen chemistry model is assumed, the following formula for the wall heat flux is finally obtained substituting Eq. (25) in Eq. (24):

$$q_w = \frac{u_\tau \rho \overline{C_p} T \ln\left(\frac{T}{T_w}\right)}{2.1 \ln(y^+) + 2.5} \tag{26}$$

from which we can see how the u_τ, which is given by Eq. (20) in the original formulation, affects the resulting wall heat flux both linearly, by appearing at the numerator, and logarithmically, entering in the definition of y^+. From the modeled q_w, a turbulent thermal diffusivity at the wall is obtained as

$$\alpha_{t,w} = \frac{q_w}{C_{p,w} \frac{\partial \widetilde{T}}{\partial y}} - \bar{\alpha}_w \tag{27}$$

4.3. Wall-coupled models (group C)

This class of models retain the mutual interaction between velocity and temperature near the wall due to chemistry and compressible effects. The model analyzed in the present work is the one of Cabrit and Nicoud [13] derived from a DNS analysis of a turbulent reactive channel flow, for which the following system of equations is derived by modeling the wall heat flux and the wall shear stress:

$$\frac{2}{A}\left(\sqrt{D} - \sqrt{D - Au^+}\right) = \frac{1}{\kappa}\ln(y^+) + C \tag{28}$$

$$T^+ = \frac{1 - D}{B_q} + \frac{A}{B_q}u^+ \tag{29}$$

being C a model constant equal to 5.5, $B_q = T_\tau/T_w$ and

$$A = \frac{C_{p,w}B_q}{C_{p,w}/Pr_t + \frac{1}{Sc_t}\sum_k dY_k/dT|_{eq}\Delta h^0_{f,k}}$$

$$\frac{1 - D}{B_q} = K(Pr_w) = \beta - Pr_tC + \left(\frac{Pr_t}{\kappa} - 2.12\right)(1 - 2\ln(20))$$

$$\beta = \left(3.85Pr_w^{\frac{1}{3}} - 1.3\right)^2 + 2.12\ln(Pr_w)$$

The previous system is solved for T_τ and u_τ by expressing $T^+ = (T_w - \widetilde{T}_P)/T_\tau$ in Eq. (29), $y^+ = \Delta y_P u_\tau/\nu_w$ and $u^+ = \widetilde{u}_P/u_\tau$ in Eq. (28), and thus is based on the outer flow conditions at the last node P and on the wall values as input quantities. A wall heat flux is then calculated as $q_w = (\rho_w C_{p,w}T_\tau)u_\tau$ and the $\alpha_{t,w}$ is finally derived from Eq. (27). The cited model has already found applications in rocket engines relevant conditions, both in its frozen [33] and reacting [26] form. Note that in the former case, the coefficient A reduces to Pr_tB_q.

From the previous description, it follows that for both classes A and B of wall functions, the $\alpha_{t,w}$ depends on an external definition of u_τ, the

26

latter directly impacting the evaluation of y^+ and thus $\nu_{t,w}$ for group A, and entering in the evaluation of the q_w for group B. Wall-coupled models C, on the other hand, do not have such dependence, providing u_τ and T_τ as a solution of the coupling between the kinematic and the thermal boundary layer, which in the case of Cabrit and Nicoud is represented by Eqs. (28)-(29). The modeled skin friction velocity, however, generally obtained from Eq. (20) in the standard wall function approach, depends on the near wall turbulent kinetic energy k_P, which is given by the solution of its transport equation at the last node before the wall

$$
\frac{\partial(\bar{\rho}_P k_P)}{\partial t} + \frac{\partial(\bar{\rho}_P \widetilde{\mathbf{u}}_{i,P} k_P)}{\partial \mathbf{x}_i} = \frac{\partial}{\partial \mathbf{x}_i}\left[\left(\bar{\mu}_P + \frac{\bar{\rho}_P \nu_{t,P}}{\sigma_k}\right)\frac{\partial k_P}{\partial \mathbf{x}_i}\right] + \\
+ \bar{\rho}_P P_{k,P} - \frac{2}{3}\bar{\rho}_P \frac{\partial \widetilde{\mathbf{u}}_{i,P}}{\partial \mathbf{x}_i} k_P - \bar{\rho}_P \epsilon_P.
\tag{30}
$$

In the above equation σ_k is a model constant equal to 1 while ϵ_P and $P_{k,P}$ are the turbulent dissipation rate and turbulent production, respectively, which need to be modeled. The modelization of these terms is independent on the employed wall function and applies to all the groups A, B and C. However, a stronger influence of the chosen near-wall turbulent modeling is expected for the models within the groups A and B rather than the ones in C, given the mentioned dependence of the former groups on Eq. (30). For group C, Eq. (30) is still solved but it doesn't directly impact the wall heat flux. The next section, therefore, describes how the two mentioned turbulent terms are modeled, especially in case of significant variation of properties across the boundary layer.

4.4. Near wall turbulence modeling

The near-wall modeling employed in the following wall modeled simulations is now presented. It is inspired by the methods proposed by Launder and Spalding and the improved model of Chieng and Launder as described by Bredberg [11], which consist in

- Solving the momentum equation, Eq. (13), with a modified viscosity in the near wall region

- Solving the turbulent kinetic energy equation in the near wall region, Eq. (30), with modified expressions for the production and dissipation terms obtained from integral considerations over the volume of the last cell before the wall

The main difference is that in our wall modeled framework the production $P_{k,P}$ and the dissipation ϵ_P terms are not given by integral expressions but rather by local values

$$\epsilon_P = \frac{u_\tau^3}{\kappa \Delta y_P} \qquad P_{k,P} = (\nu_w + \nu_{t,w})\frac{d\widetilde{u}}{dy}\frac{u_\tau}{\kappa \Delta y_P} \tag{31}$$

where the u_τ is retrieved from Eq. (20) with a predicted value of turbulent kinetic energy. The expression of $P_{k,P}$ in Eq. (31) strictly comes from the definition of turbulent production in the near wall region, given by

$$P_{k,P} = -\widetilde{u''v''}\frac{d\widetilde{u}}{dy} = u_\tau^2 \frac{u_\tau}{\kappa \Delta y_P} \tag{32}$$

supposed x and y the streamwise and crosswise directions, respectively, and being $\widetilde{u''v''}$ a component of the Reynolds stress tensor. The latter can be written as u_τ^2 if the constant shear stress assumption is employed together

28

with the assumption of constant properties across the boundary layer ($\tau_{xy,P} = -\rho_P \widetilde{u''v''} = \rho_w u_\tau^2 = \tau_w$, with $\rho_P = \rho_w$). The quantity u_τ^2 is then written as τ_w/ρ_w, where the corrected wall shear stress $\tau_w = (\mu_w + \mu_{t,w})\frac{d\widetilde{u}}{dy}$ is introduced. The term $\frac{d\widetilde{u}}{dy}$ in Eq. (32), on the other hand, is expressed as $\frac{u_\tau}{\kappa \Delta y_P}$ by assuming the logarithmic law of the wall for the velocity. The near wall turbulent dissipation ϵ_P, on the other hand, is derived by imposing dissipation equal to production, with the latter given by Eq. (32). The expressions in Eq. (31) are then fed inside Eq. (30) to update the predicted value of k_P.

The previous expressions are derived considering constant properties across the boundary layer, i.e $\rho_P = \rho_w$. Under rocket-relevant conditions, however, strong temperature gradients are expected on the combustion chamber walls, causing a substantial variation of properties across the boundary layer. As a consequence, the ratio of densities between the first off grid node and the wall is generally different from unity. In the work of Cabrit and Nicoud [13], it is shown how the previous expressions must be corrected whenever this is the case. In particular, the resolved wall normal velocity gradient is shown to take the form $\frac{d\widetilde{u}}{dy} = \left(\frac{\rho_w}{\rho_P}\right)^{1/2} \frac{u_\tau}{\kappa \Delta y_P}$. Moreover, the turbulent kinetic energy at the last node reads

$$k_P = \frac{\rho_w}{\rho_P} \frac{u_\tau^2}{\sqrt{C_\mu}} \tag{33}$$

Equation (33) is a consequence of the assumption of constant shear stress in the boundary layer, and of the experimental relation between the turbulent shear stress and the turbulent energy, valid in the inertial logarithmic region of a boundary layer [13],

$$C_\mu^{1/2} k_P = -\widetilde{u''v''}. \tag{34}$$

The turbulent dissipation rate and the turbulent production terms accord-

ingly become

$$\epsilon_P = \left(\frac{\rho_w}{\rho_P}\right)^{3/2} \frac{u_\tau^3}{\kappa \Delta y_P} \qquad P_{k,P} = (\nu_w + \nu_{t,w}) \left(\frac{\rho_w}{\rho_P}\right)^{3/2} \frac{d\widetilde{u}}{dy} \frac{u_\tau}{\kappa \Delta y_P} \qquad (35)$$

Note that in [13] a factor $(\rho_P/\rho_w)^{1/2}$ appears in the expression of ϵ_P. All the above expressions reduce to the standard definitions previosuly given when $\rho_P = \rho_w$. Eq. (33), in particular, leads to a new definition of u_τ based on the local turbulent energy, which accounts for the variation of properties across the boundary layer

$$u_\tau = \left(\frac{\rho_P}{\rho_w}\right)^{1/2} C_\mu^{1/4} \sqrt{k_P} \qquad (36)$$

5. Results

In this section, results of the wall modeled numerical simulations of an experimental GOx/GCH4 single-injector combustor are presented. The facility is described in the next section. The rationale is to validate the proposed numerical framework in a 2D setting and then move to 3D simulations, given the lower computational cost associated to axis-symmetric grids.

5.1. Test case and numerical setup

In the present study the experimental configuration developed at the Technical University of Munich is investigated. The facility features a single-element GCH4/GOx combustor [27] capacitively cooled with a square cross section of 12 mm × 12 mm. Experimental data are provided for the axial pressure and the wall heat flux. The latter is reconstructed with an inverse method [29] based on data collected by thermocouples along the chamber. Propellants are injected through a coaxial injector at the nominal conditions

cited in section 2.2. The chosen operating point consists in a nominal chamber pressure of 20 bar and an Oxidizer to Fuel Ratio (ROF) of 2.6. The oxidizer and fuel mass flow rates are 0.0045 kg/s and 0.0017 kg/s, respectively. The computational domains employed in the next sections are truncated at the nozzle inlet since we operate in a low-Mach number framework. The injector channels are not included in the computational mesh as also done in the LES simulations by Zips et al. [31]: inlets are therefore patched at the faceplate and adiabatic conditions are imposed on the post-tip and the plate walls; a temperature profile extracted from the experiments is applied over all the chamber walls as a boundary condition. All the simulations are performed in the context of a modified version of the open source software package OpenFOAM [70], implementing the models previously described and already employed in previous works [43, 44, 50, 71, 53, 72]. The pressure-based PIMPLE [73] solution algorithm is used to handle the pressure-velocity coupling. Second order schemes are chosen for the spatial discretization while a first order implicit Euler scheme is used for time integration.Table (1) reports a summary of the simulations performed. The labels employed apply both for the 2D and the 3D simulations which will be presented in the next sections. The different wall functions for the $\alpha_{t,w}$ are denoted by A, B or C according to sec. 4. Therefore, $\alpha_{t,w}$ is retrieved from the $\nu_{t,w}$ for the simulations employing the Reynolds analogy (group A) and from the modeled q_w for the wall function formulations of the groups B and C, according to Eq. (27). The $\nu_{t,w}$ is obtained from Eq. (22) for all the cases. All the simulations employ the frozen combustion model and the standard $k - \epsilon$ as turbulence model. The latter has shown better performance with respect to others for

31

Label	$\alpha_{t,w}$ group	WF Model	u_τ	$\epsilon_P - P_{k,P}$
R-CP	A	Reynolds analogy	Eq. (20)	Eqs. (31)
HR-CP	B	Han and Reitz	Eq. (20)	Eqs. (31)
CN-CP	C	Cabrit and Nicoud	-	Eqs. (31)
R-VP	A	Reynolds analogy	Eq. (36)	Eqs. (35)
HR-VP	B	Han and Reitz	Eq. (36)	Eqs. (35)
CN-VP	C	Cabrit and Nicoud	-	Eqs. (35)

Table 1: Labels of the next 2D and 3D simulations of the TUM single-injector. CP and VP respectively denote the constant and variable property assumptions used to model the near-wall turbulent quantities according to sec. 4.4

the considered thermodynamic conditions [30, 41].

A Neumann condition is used for the turbulent kinetic energy at the wall while turbulent production and dissipation rate at the last node are obtained from Eqs. (31) or Eqs. (35), according to the employed assumption of constant (CP) or variable (VP) properties across the boundary layer. The wall heat flux is directly obtained from Eq. (26) for the model of Han and Reitz while in Cabrit and Nicoud it is obtained as $q_w = (\rho_w C_{p,w} T_\tau) u_\tau$, where u_τ and T_τ come from the solution of the coupled system of Eqs. (28)-(29). A Brent solution algorithm [74] is used for the solution of the non-linear equation in u_τ arising from the cited system. For the simulations employing the Reynolds analogy and the model of Han and Reitz the skin friction velocity is obtained from the local turbulent kinetic energy according to Eq. (20) or Eq. (36), depending on the CP or the VP assumption. The Pr_t entering both in the diffusion term of the transport equations and in evaluation of the wall functions A

and C is conventionally set to 0.85. For the model of Han and Reitz its value is calculated a-posteriori as a function of the average y^+ according to the polynomial fitting proposed by the authors [16]. For the grids employed in this work it was shown to sligthly change from $\simeq 0.85$, thus allowing a consistent comparison with the other models. No slip conditions are imposed on the walls and a temperature profile extracted from experiments is applied on the chamber wall.

5.2. Wall modeled 2D simulations

Firstly a mesh resolution analysis is conducted in order to ensure the grid independence of the next results. A regular and equispaced baseline mesh of 548×52 computational volumes is therefore doubled and halved in the number of nodes both in the longitudinal and radial directions in order to obtain a finer and a coarser grid, respectively, with same spatial grading. The last cell width of the baseline mesh measures 133.6 μm. Figure 3 reports line plots for the mean temperature and temperature fluctuations sampled along the chamber axis for the three grids employed and the mean temperature field ensuing from the baseline mesh.

Results in Fig. 3(a) show a steeper temperature increment in the first part of the chamber between the coarse and the base mesh. This is due to the finer resolution provided by the baseline grid, which causes an anticipated radial expansion of the flame due to the higher resolved degree of mixing. This ultimately reflects in a shorter distance of the re-attachment point from the injection plate. No appreciable differences are observed between the baseline and fine grids, both showing similar trends. According to this, the former is chosen for the following 2D analysis as a good compromise between
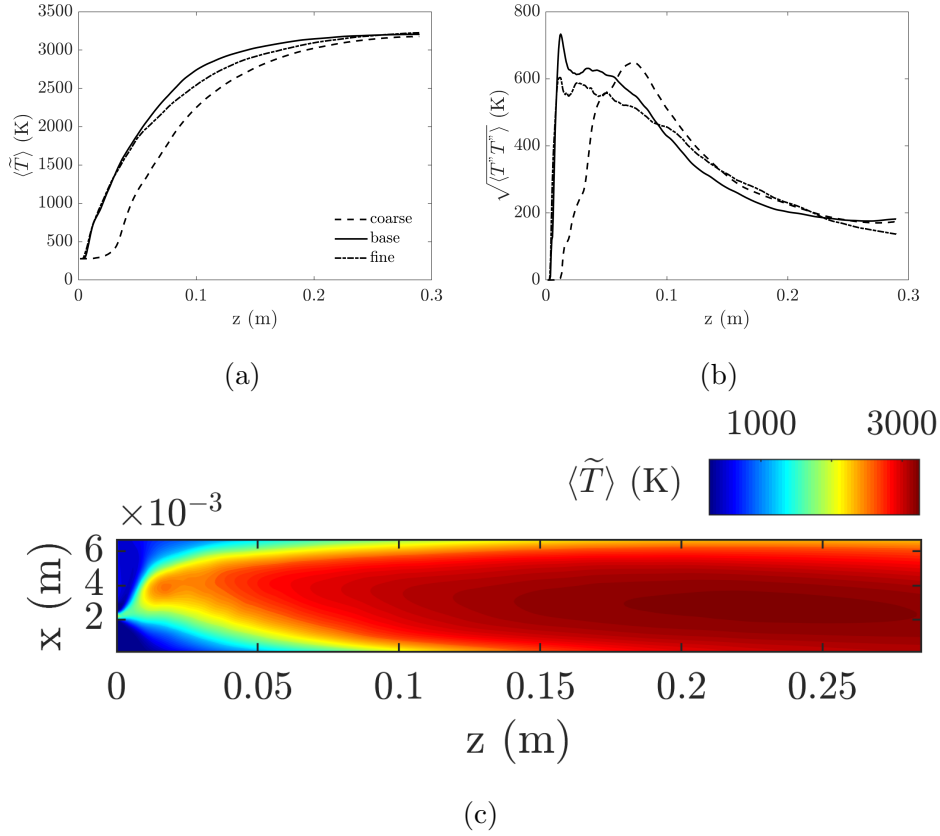
Figure 3: Mesh convergence analysis on the 2D wall modeled simulations: mean (a) and root mean square (b) of temperature sampled along the chamber axis for the coarse, base and fine grid; (c) mean temperature field from the baseline mesh. View is stretched by a factor 0.2 in streamwise direction.

reliability of the results and computational cost. A first comparison between the three classes of models is provided in Fig. 4 in terms of wall heat flux and wall pressure. Please note that the experimental set denoted as Celano et al. 2016 (method 2b), in Fig. 4(a) and in the following, indeed refers to the experimental profile used in Zips et al. [31] for a similar comparison, which slightly differs from the one found in the original reference [27].

34
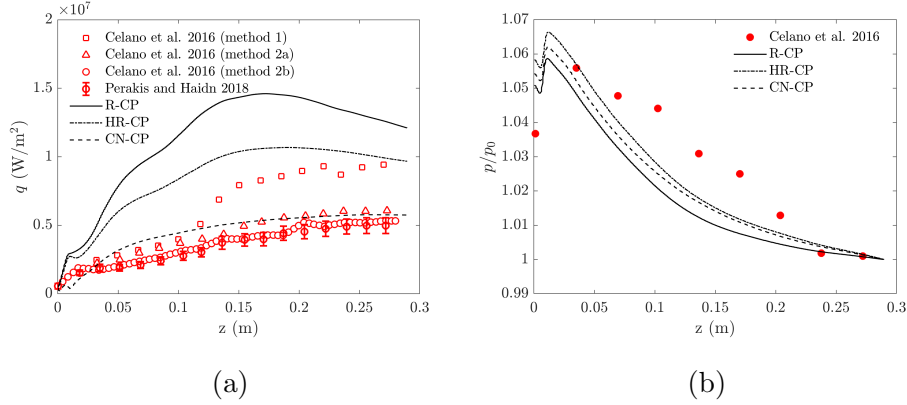
Figure 4: Wall heat flux (a) and pressure at the wall (b) from the 2D wall modeled simulations of the TUM single-injector.

As observable from Fig. 4(a), R-CP and HR-CP predict a similar trend for the wall heat flux although they drastically overestimate the experimental results from $z \simeq 0.04$ m on. For the former this could depend on the chosen law for $\nu_{t,w}$ (Eq. (22) in this case) which directly affects the $\alpha_{t,w}$, and on the given value of Pr_t. The latter, however, is not expected to have such an influence to justify the considerable differences with the experiments observed in Fig. 4(a), as also stated in [41]. Different laws for $\nu_{t,w}$ could indeed be tested in order to obtain better results; while interesting, a similar analysis would be beyond the purpose of the present analysis. The CN-CP on the other hand predicts a wall heat flux in good agreement with the available experimental data on the entire chamber length, except for the region above the injection plate, where some discrepancies are observed for $z < 0.04$ m. The latter could be due to the limitations of the model, which was shown to perform better with respect to the standard wall laws for wall bounded flows in which the gases temperature T_{gas} is much higher than the wall temperature

35

T_{wall}, in particular for $T_{gas}/T_{wall} > 3$ [13, 33]. Fig. 5 indeed shows how this ratio is below this lower bound up to the mentioned abscissa.
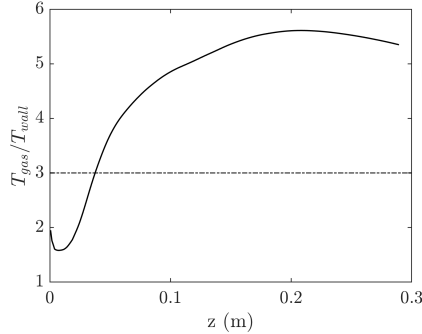
Figure 5: T_{gas}/T_{wall} for the CN-CP simulation. T_{gas} is assumed as the near wall temperature.

An explanation for the trends observed in Fig. 4(a), indeed, can be found observing the quantities affecting the wall heat flux predicted by each model. For both R-CP and HR-CP the heat flux depends on u_τ, which impacts (i) the model of Han and Reitz both explicitly at the numerator of Eq. (26) and both implicitly on the evaluation of y^+ and (ii) the Reynolds analogy model on the evaluation of y^+ and thus $\nu_{t,w}$ according to Eq. (22). The skin friction velocity, however, in both cases is retrieved from the local turbulent kinetic according to Eq. (20). That is, both the described models are strongly dependent on the near wall modeling, which is kept the same for the three test cases. The mentioned dependence, on the other hand, is not present in the model of Cabrit and Nicoud which predicts a significantly different trend with respect to the other two. In this model in fact the u_τ is obtained as a solution of the coupling system of Eqs. (28)-(29), and thus is not directly affected by the near wall modeling. This suggests that the similarities between R-CP

36

and HR-CP and the gap with CN-CP could indeed be explained in terms of near wall turbulence modeling. In this first analysis the latter is based on the assumption of constant properties across the boundary layer. In the next sections the effect of this assumption is investigated by employing Eqs. (35) instead of Eqs. (31) for the near wall turbulent production and dissipation, and Eq. (36) instead of Eq. (20) for the skin friction velocity.

5.3. A-priori analysis of friction velocity scaling

Before assessing the effect of the variable properties assumption across the boundary layer on the the wall heat flux, we investigate the effect of the density ratio appearing in the definition of u_τ given by Eq. (36) in an a-priori fashion. To this end we perform an additional wall-resolved simulation (denoted in the following as WR-F) of the same test case using the Launder-Sharma low-Reynolds turbulence model [75]. A grid convergence analysis, schematically reported in Fig. 6, is carried out to find the last cell width Δ ensuring $y^+ \leq 1$ along the chamber wall, resulting in $\Delta = 0.5$ μm. The skin friction as obtained from Eq. (20) and Eq. (36) along the chamber length and at different distances from the wall (i.e for increasing values of $\Delta y_P/\Delta$) is then compared with its nominal definition based on the wall-resolved wall shear stress, considered as a reference solution for this analysis. Results are displayed in Fig. 7(a).

As can be observed from Fig. 7(a) as we move far from the wall, and thus for increasing values of $\Delta y_P/\Delta$, the definition of u_τ from Eq. (20) overestimates the one obtained from the wall resolved simulation. The skin friction velocities predicted by Eq. (36) on the other hand asymptotically collapse on it. This is a result of the scaling $u_\tau \sim (\rho_P k_P)^{1/2}$: as we move far from
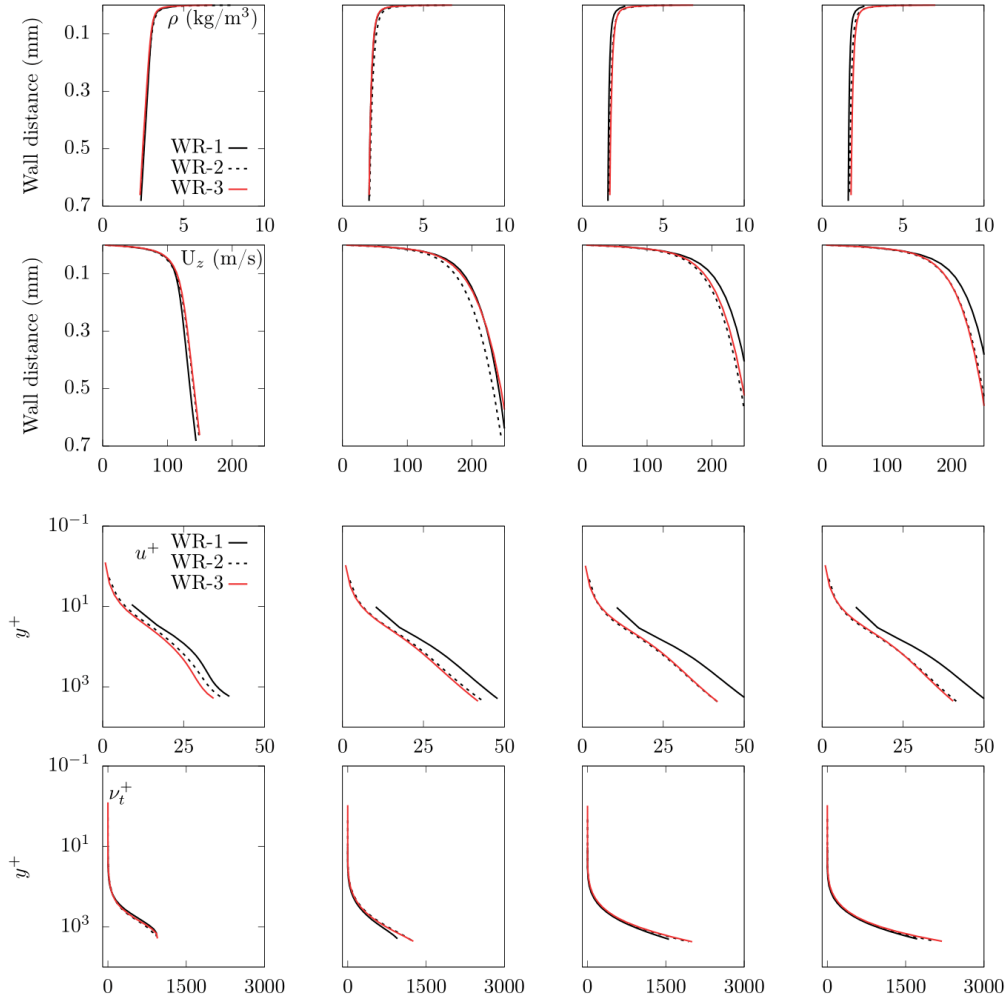
37

Figure 6: Mesh convergence analysis for the wall-resolved simulation of the single-injector chamber: radially sampled values of selected quantities in proximity of the upper chamber wall at four sections along the axis ($z = 0.025$, $z = 0.125$, $z = 0.225$ and $z = 0.275$ m) for three grids, namely WR-1, WR-2 and WR-3, with same number of cells along the axial (1.5K) and radial direction (64) but different grading towards the wall.
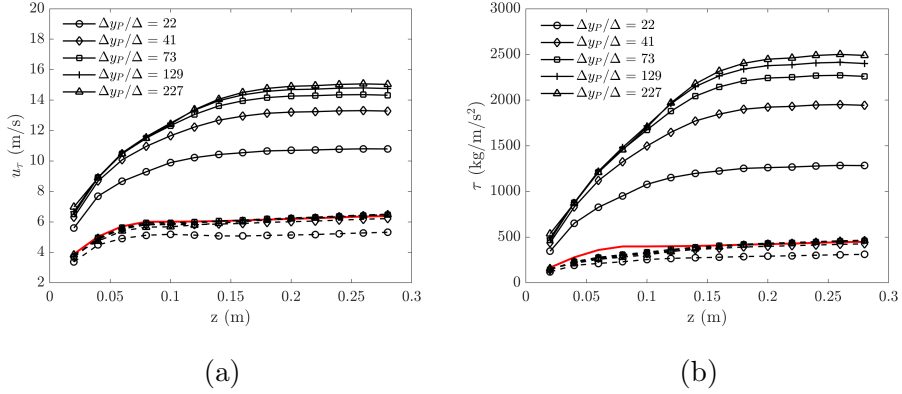
Figure 7: Panel (a): a-priori analysis of Eq. (36) on the wall resolved grid: u_τ from Eq. (20) (solid lines); u_τ from Eq. (36) (dashed lines); u_τ from WR-F (red line). Panel (b): turbulent shear stress ($\tau_{xy,P}$) reconstructed at different distances from the wall and compared with the wall shear stress ($\tau_w = \rho_w u_\tau^2$, red line): $\tau_{xy,P} = \rho_w C_\mu^{1/2} k_P$, solid lines; $\tau_{xy,P} = \rho_P C_\mu^{1/2} k_P$ dashed lines.

the wall, in fact, an increase in the turbulent kinetic energy is observed, associated to a decrease in the gas density due to higher temperature. This is shown for istance in Fig. 8, where radial profiles of $k^+ = k/u_\tau^2$ and $\rho^+ = \rho/\rho_w$, normalized with the skin friction velocity based on the wall-resolved shear stress, are plotted as a function of y^+ for a section of the chamber where the flow can be considered fully developed.

The quantity $\rho_P k_P$ is indeed proportional to the local shear stress (which is constant across the boundary layer under the equilibrium assumption) by mean of the constant C_μ from Eq. (34). In Eq. (20) the observed increase of k_P in the inner wall region is not compensated by ρ_P, thus causing a significant overestimation of the shear stress in the boundary layer, as observed in Fig. 7(b). The definition of skin friction velocity given by Eq. (20), therefore,

39
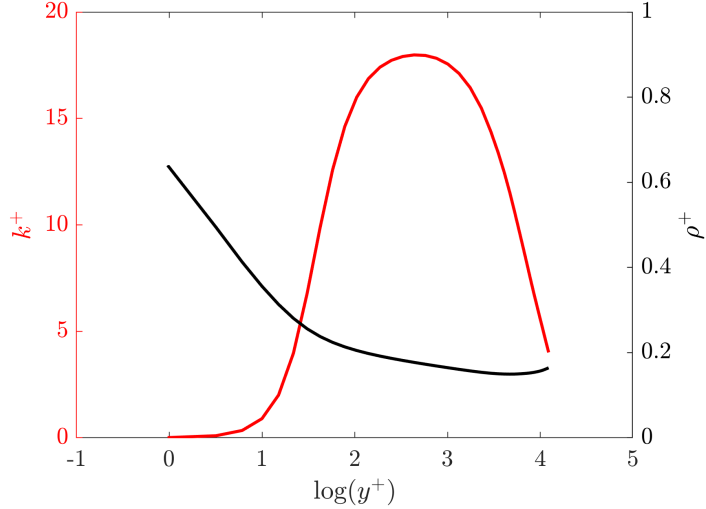
Figure 8: Radial profiles of density and turbulent kinetic energy along a cross section of the chamber. Length is in wall units.

is valid only as long as $\rho_P/\rho_w \simeq 1$. If this ratio exhibits significant deviations from unity, the standard definition of skin friction given by Eq. (20) violates the underlying assumption of constant shear stress across the boundary layer, and as a result the equilibrium boundary layer assumption on which the wall modeled framework described in sec. 4.4 is based. This happening whenever a thermal boundary condition is applied in a wall-modeled context, as previously shown in Fig. 5.

5.4. Effect of variable properties assumption across the boundary layer

The three classes of models A, B and C are now tested with the assumption of variable properties across the boundary layer which causes near wall turbulent quantities to be modeled according to Eqs. (35) rather than Eqs. (31) and provides a correction on the definition of the skin friction ve-

locity as given by Eq. (36). Results compared with experiments are displayed in Fig. 9.

(a)   (b)
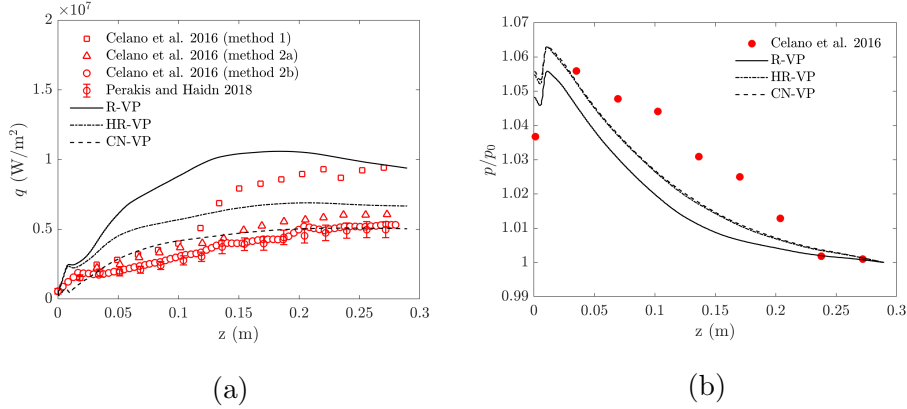
Figure 9: Wall heat flux (a) and pressure at the wall (b) from the 2D wall modeled simulations of the TUM single-injector under the assumption of variable density across the boundary layer.

As observable from Fig. 9(a), wall heat fluxes ensuing from R-VP and HR-VP are now considerably lower compared to R-CP and HR-CP. The model based on the Reynolds analogy, however, still results in an overestimation of the experimental results. The differences with respect to the values in Fig. (4)(a) in particular are due the lower value of u_τ predicted by Eq. (36) with respect to Eq. (20), and showed in Fig. 10.

Interestingly from Fig. 11, reporting wall quantites from selected wall functions, the model of Cabrit and Nicoud is slightly affected by the assumption of variable properties across the boundary layer. This is in accordance with the previous observations: the density ratio appearing in Eq. (36), in fact, was shown to be necessary to predict a correct shear stress in the boundary layer, consistently with the equilibrium hypothesis; in the derivation of

41
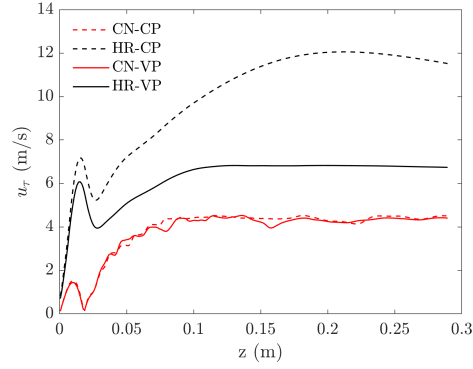
Figure 10: Effect of variable properties assumption on the skin friction velocity for the model of Han and Reitz and Cabrit and Nicoud.
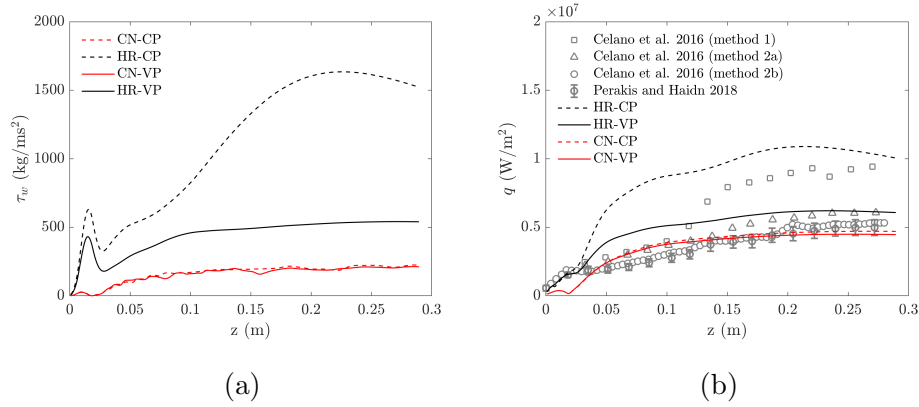

Figure 11: Panel (a): effect of variable properties assumption on the wall shear stress for the model of Han and Reitz and Cabrit and Nicoud. Panel (b): closer look at the wall heat flux from HR-CP,HR-VP,CN-CP and CN-VP. The data plotted come from simulations on the coarse grid.

the coupled model, however, the mentioned equilibrium assumption is implicitly retained, and the shear stress consequently calculated. Therefore, for the mentioned model, Eqs (35) only affect the near wall fields without directly entering in the evaluation of τ_w or q_w. The groups A and B, on the other

42

hand, require an external definiton of skin friction velocity, and thus show a stronger dependence on the employed near wall modeling. This observation is also supported by the work of Rakopoulos et al. [18], where the model of Han and Reitz is applied to the simulation of an internal combustion engine. The cited dependence, in particular, strongly alters the predicted wall heat flux. To further assess the results of Fig. 9, the response of these two models to different refinement degrees is investigated in the next section.

5.5. Response of HR-VP and CN-VP to different mesh refinements

The models of Han and Reitz and Cabrit and Nicoud are now tested on the grids of Fig. 3 to investigate the effect of different y^+. Figure 12 reports the wall heat flux obtained with the cited models on the mentioned grids. No relevant differences are observed between the base and fine grid for both the models. A slight increment of the wall heat flux right after the injection plate is indeed observed between the coarse and base grid, together with a shift of the local peak. This is however in agreement with the observations made on the grid convergence analysis of Fig. 3. As a further analysis on this point, Fig. 13(a) displays the average values of y^+ on the chamber wall for the HR-VP and the CN-VP, while Fig. 13(b) the respective u_τ profiles for the HR-VP.

5.6. Wall modeled 3D simulations

The wall modeled framework and wall function models described in the previous sections are now applied to 3D simulations of the single-injector chamber. A baseline mesh of 85K cells is first used with a last cell size fixed by the previous mesh sensitivity analysis, while a finer mesh of 680K finite
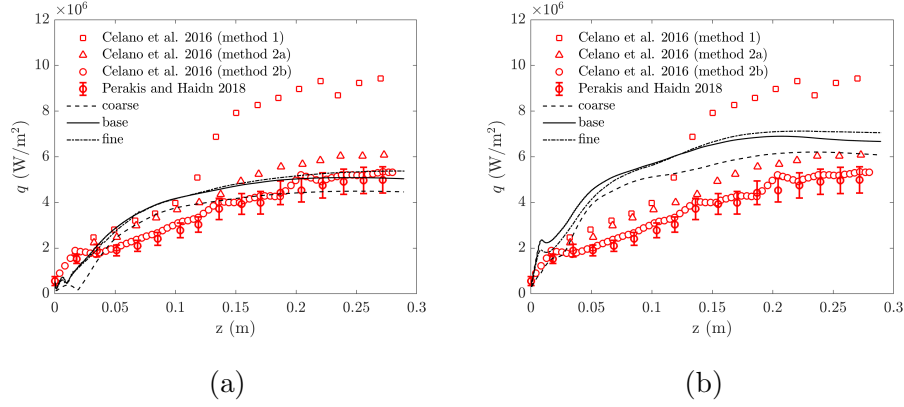
43

Figure 12: Wall heat flux profiles obtained with the model of Cabrit and Nicoud (a) and Hand and Reitz (b) on different grids.
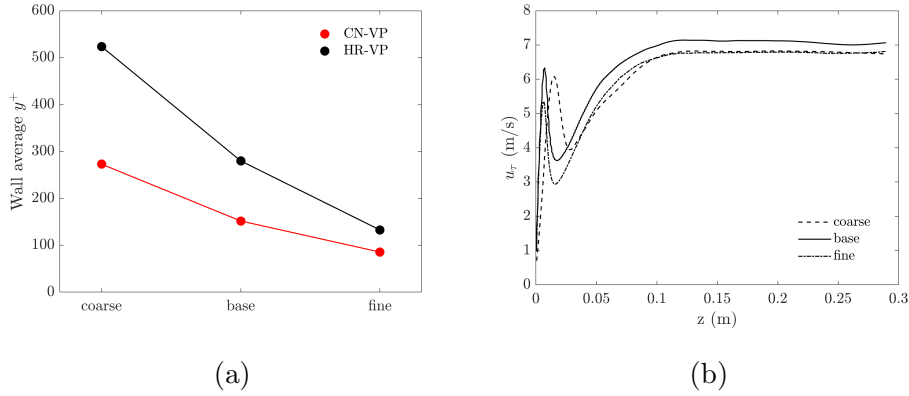

Figure 13: Average y^+ for HR-VP and CN-VP (a) and skin friction velocity for HR-VP (b) on the different grids.

volumes is then obtained by halving each computation cell in each direction, to further assess the grid sensitivity of the selected models in a 3D context. The same boundary and inlet conditions of the 2D case apply. The near wall turbulence modeling is described by Eqs. (35) based on the analysis of the previous section and the frozen combustion model is used.

44

A comparison between the numerical and experimental OH^* emission measurement from Winter et al. [76] is performed as a validation of the numerical results. The simulated OH^* signal is modeled from the OH concentration according to the method of Fiala and Sattelmayer [77] similarly to Zips et al. [31]

$$[OH^*] = [OH]exp\left(\frac{hcN_A}{\lambda RT}\right) \tag{37}$$

where h is the Planck constant, c the speed of light, $\lambda = 308$ nm, N_A the Avogadro number and R the gas constant. The OH^* field is then averaged in time over an interval of 40 ms, which is equivalent to about 960 flow through times D_{O_2}/U_{O_2}, being D_{O_2} the oxygen inlet diameter and U_{O_2} the oxygen inlet velocity. Line of sight integration of the OH^* signal is performed by averaging the mean OH^* field ($\langle OH^* \rangle$) over a set of equispaced longitudinal slices taken along the chamber length for a total of 200 slices. Contours of $\langle OH^* \rangle$ normalized with respect to its maximum value in the field are showed between 0.1 and 0.9 in Fig. 14.

The experimental OH^* chemiluminescence is weak up to $4 - 5D_{O_2}$, that is $15 - 20$ mm away from the injection plate, after which the flame thickens and a sudden increase in OH^* is observed. In the numerical simulation this behavior is qualitatively well captured, although the mentioned expansion starts earlier at around 10 mm. Also the luminescence is less bright than the one predicted by the experiments, being the maximum contour level attained towards the outlet section . The flame opening angle, however, is quite well reproduced, suggesting a good mixing level predicted by the simulation [31].
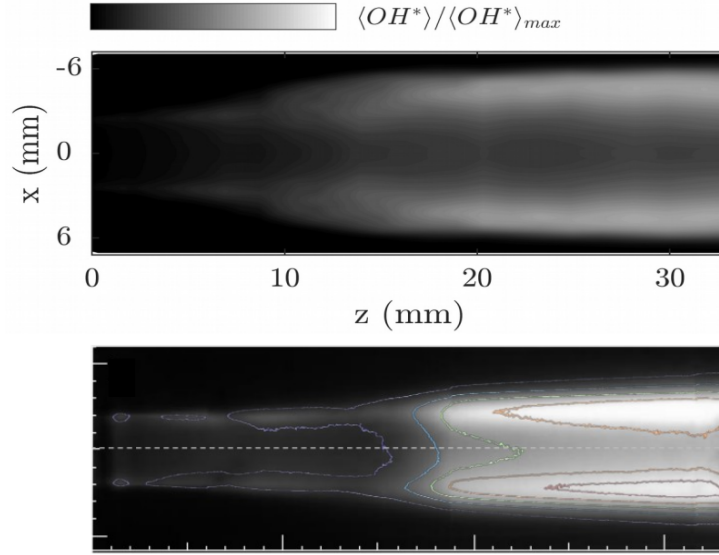
Figure 14: OH^* numerical emission image (top) compared with the experimental one (bottom). Figure taken from [76].

5.7. Wall function models comparison

The comparison with the experiments is performed by an azimuthal average of the instantaneous wall profiles which are then averaged in time. Figure 15 reports a comparison between the wall heat flux from 3D simulations with the models of Han and Reitz and Cabrit and Nicoud on the employed 3D grids. The same labeling strategy of the 2D simulations is used. A substantial agreement with the observations made on the 2D setting, is also found in the 3D context.

Figure 16 further investigates the difference between the two models, by displaying wall heat flux time-averaged profiles at selected azimuthal positions on the upper chamber wall from the baseline mesh, corresponding to the left and right corners and to the centerline of the chamber.
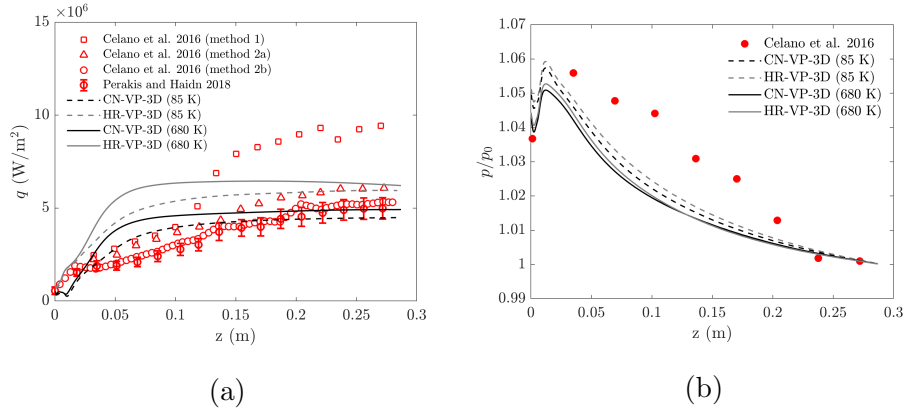
Figure 15: Azimuthal-averaged wall heat flux profiles (a) and centerline pressure at the wall (b) from 3D simulations of the TUM single-injector.
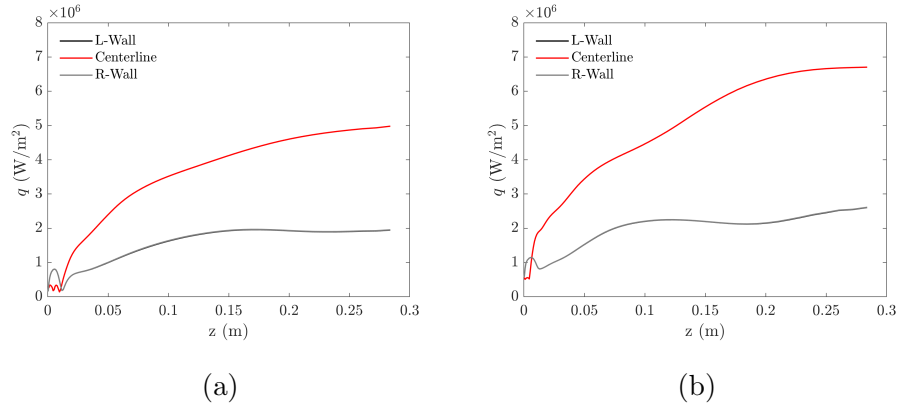

Figure 16: Time-averaged wall heat flux sampled at the corners of the chamber and at the centerline for the CN-VP (a) and the HR-VP (b).

A colder near-wall flow is observed directly above the injector as seen from the lower values of wall heat flux at the centerline with respect to the corners. Moreover, the steeper slope observed in the centerline profiles suggests a hotter flame impinging the wall with respect to the corners. This is also confirmed by looking at the azimuthal profiles of wall heat flux at

47

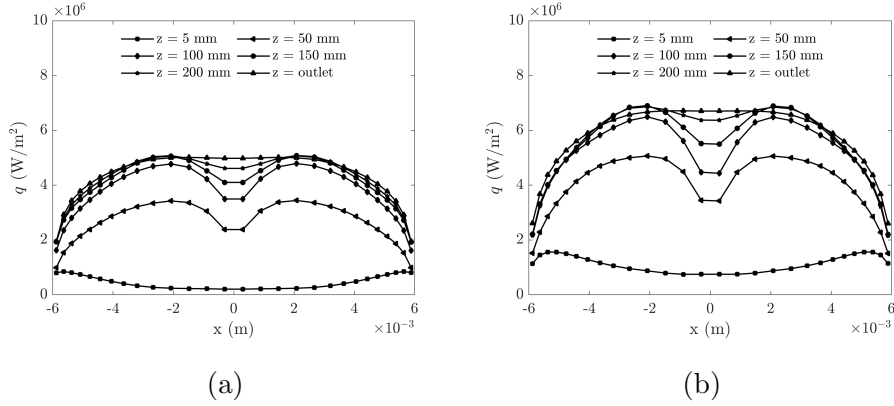different axis locations shown in Fig. 17.

Figure 17: Azimuthal profiles of wall heat flux for the CN-VP (a) and the HR-VP (b) test case.

5.8. Comprehensive comparison with literature LES and experimental data

In this section the results obtained from the previous 3D simulation employing the coupled wall function model are compared with results taken from the literature. In particular the simulations by Zips et al. [31] and Maestro et al. [33] are considered as terms of comparison. The notation adopted in this section discerns between wall resolved (WR-), wall modeled (WM-) LES simulations and a hybrid RANS/LES approach, namely Improved Delayed Detached Eddy Simulation (IDDES). Some details of such simulations are reported below, specifically focused on the employed wall modeling. For more details the interested reader is referred to the respective articles.

WM-LES-AVBP [33] The 3D simulation of Maestro et al. is characterized by an average y^+ on the chamber walls of 45. The employed combustion model is based on a direct integration of the chemistry and a thickened

flame concept [78] extended to non-premixed combustion. The wall heat flux is calculated with the model of Cabrit and Nicoud in the form reported in sec. 4, thus neglecting chemical reactions in the boundary layer.

WR-LES [31] The chamber length of the wall resolved LES is truncated at 102.5 mm. Wall heat flux data are thefore limited to that abscissa in the next plots. The WALE SGS model [79] is employed for the near wall modeling. The combustion model is based on a tabulated flamelet approach where the composition is kept frozen to adiabatic conditions while heat is progressively extracted from the mixture, thus making it equivalent to our frozen approach described in sec. 2.

WM-LES [31] As for Maestro at al., the LES by Zips at al. is characterized by an average y^+ on the wall of $\simeq 47$. Near wall modeling is based on an approximate wall law proposed by Spalding, representing a fit of viscous sublayer, buffer region and logarithmic layer

$$y^+ = u^+ + \frac{1}{E}\left[e^{\kappa u^+} - 1 - \kappa u^+ - \frac{1}{2}(\kappa u^+)^2 - \frac{1}{6}(\kappa u^+)^3\right] \qquad (38)$$

Eq. (38) is iteratively solved in u_τ with a Newton algorithm, providing a value of skin friction velocity on the last nodes before the wall. A turbulent viscosity $\nu_{t,P}$ is then retrieved by integrating the momentum equation in the near wall region, written under the assumptions of incompressible flow and zero streamwise pressure gradient and reading

$$\frac{1}{\bar{\rho}}\frac{d\tau_{xy}}{dy} = \frac{d}{dy}\left[(\bar{\nu} + \nu_t)\frac{d\widetilde{u}}{dy}\right] = 0, \qquad (39)$$

49

between the first off grid node and the wall, leading to

$$(\bar{\nu}_P + \nu_{t,P})\frac{d\widetilde{u}}{dy} = u_\tau^2 \tag{40}$$

where u_τ comes from the solution of Eq. (38). Equation (40) expresses the conservation of the shear stress across the boundary layer ($\tau_{xy,P} = \tau_w$), with $\rho_P = \rho_w$ according to the previous assumptions. A turbulent thermal diffusivity α_t is then derived from $\nu_{t,P}$ assuming a Pr_t equal to 0.7, in order to calculate the turbulent wall heat flux.

IDDES [31] This method allows for a $y^+ \simeq 1$ but at the same time high apect ratios towards the wall due to the RANS treatment of the the boundary layer. As a result the latter is fully resolved as in the WR-LES and the wall heat flux reduces to the molecular contribution.

Figure 18 reports the azimuthally averaged wall heat fluxes for the mentioned simulations, compared with experiments and the results obtained in the previous section. As observed, an overall similar trend is predicted by each setting. In the first 20 mm of the chamber in particular all the profiles overlap to the experiments except for the CN-VP. Between $z = 20$ and $z = 100$ mm a substantial disomogeneity is observed among the different models, with the wall modeled LES being the closest to the experimental data. All the profiles however are in good agreement with each other and with the experimental data from $z = 200$ mm till the end of the chamber. The same considerations apply for the wall heat fluxes at the center of the chamber, displayed in Fig. 19(a), while more significant deviations are observed at the corners, in Fig. 19(b). The data for the WM-LES displayed in
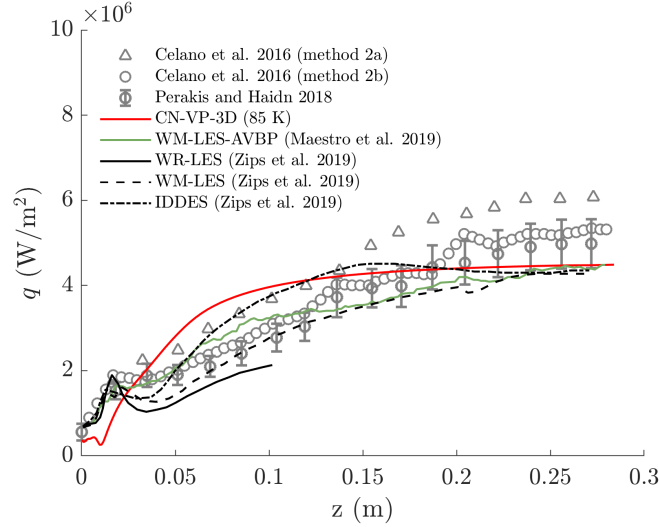
50

Figure 18: Comparison of wall heat flux profiles from 3D simulations of the TUM single-injector.

Fig. 19 were derived from the corresponding time-averaged circumferential variation err_θ of the wall heat flux reported in Zips et al. [31] and defined as

$$err_\theta = \frac{q_\theta - q_{avg}}{q_{avg}} \tag{41}$$

being q_θ the time-averaged wall heat flux at the considered azimuthal position θ (centerline or corner) and q_{avg} the mean profile plotted in Fig. 18.

6. Conclusions

This work presented an efficient numerical framework for the simulation of high-pressure turbulent flows in LRE-relevant conditions, specifically suited for wall heat flux preditions in LRE combustion chambers. The proposed framework was applied to 2D and 3D simulations of an experimental single-
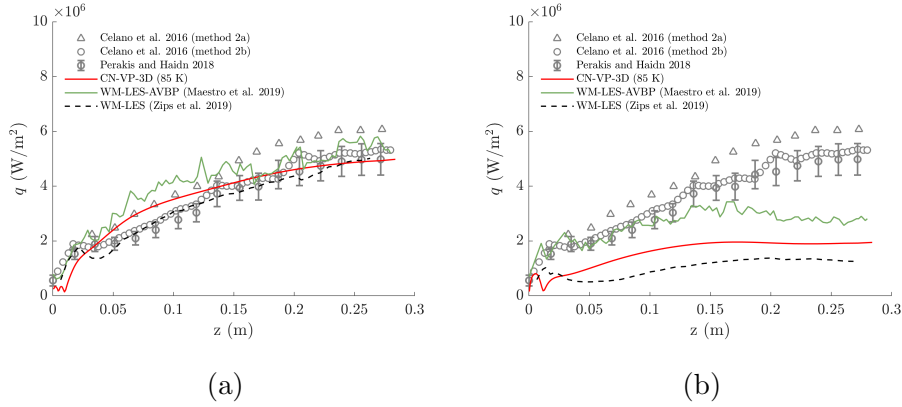
Figure 19: Comparison of wall heat flux profiles from 3D simulations of the TUM single-injector along the centerline (a) and at the edge of the chamber (b).

element gaseous oxygen-gaseous methane combustor and validated against available experimental data. In particular:

- A new non-adiabatic flamelet model was proposed in order to retain non-adiabatic effects under frozen and equilibrium chemistry conditions. The proposed model represents the easiest logical improvement to the uniform enthalpy defect subtraction method proposed in [42], which caused unphysical temperature values at the boundaries of the mixture fraction space.

- Different wall funtion models for the evaluation of the wall heat flux in a wall modeled framework were systematically implemented in a flamelet-based solver and tested in 2D and 3D URANS simulations. A version of the model of Han and Reitz [16] (originally conceived for the simulation of internal combustion engines) adapted to LRE-like conditions was proposed. Results showed that models belonging to group A and B drastically overestimate the ensuing wall heat flux when

52

used in conjunction with the constant properties assumption across the boundary layer applied to the modelization of the near-wall turbulent quantities; the coupled model of Cabrit and Nicoud, on the other hand, showed a good agreement with the experimental values independently on the chosen near-wall modeling. Some deviations from the experiments were observed in the near injector zone, where the gas-to-wall temperature ratio is below the threshold value proposed by the authors in the derivation of the model.

- An a-priori analysis of the friction velocity scaling in a wall-resolved context associated the mentioned overestimation to a violation of the equilibrium boundary layer assumption. In the case of non-neglegible properties variation in the boundary layer, a corrective density ratio is required in the definition of the skin friction velocity based on the local turbulent kinetic energy to ensure the validity of the equilibrium assumption.

- The proposed framework was shown to effectively reproduce the internal flow field of the experimental combustor under examination and showed a substantial agreement in terms of wall heat flux with results from higher fidelity simulations and available experimental data.

7. Acknowledgements

discussion on the combustion chamber test case.

8. References

[1] A. Iannetti, N. Girard, N. Ravier, E. Edeline, D. Tchou-Kien, Prometheus, a low cost LOX/CH4 engine prototype, 2017. URL https://doi.org/10.2514/6.2017-4750

[2] P. Bellomi, M. Rudnykh, S. Carapellese, D. Liuzzi, G. Caggiano, L. Arione, A. Gurtovoy, S. Lobov, V. Rachuk, E. D'Aversa, et al., Development of LM10-MIRA liquid oxygen–liquid natural gas expander cycle demonstrator engine, Progress in Propulsion Physics 11 (2019) 447–466.

[3] F. Battista, D. Ricci, M. Ferraiuolo, D. Cardillo, M. Fragiacomo, P. Natale, V. Salvatore, The HYPROB LOX-LCH4 demonstrator: status of the manufacturing and experimental activities, in: Proceedings of the 7th European Conference for Aeronautics and Space Sciences, 2017.

[4] C. Brown, Conceptual investigations for a methane-fueled expander rocket engine, in: 40th AIAA/ASME/SAE/ASEE Joint Propulsion Conference and Exhibit, 2004, p. 4210.

[5] G. P. Sutton, History of liquid propellant rocket engines, Vol. 616, American Institute of Aeronautics and Astronautics, 2005.

[6] P. Caisso, A. Souchier, C. Rothmund, P. Alliot, C. Bonhomme, W. Zinner, R. Parsley, T. Neill, S. Forde, R. Starke, et al., A liquid propulsion panorama, Acta Astronautica 65 (11-12) (2009) 1723–1737.

[7] S. Acharya, B. Baliga, K. Karki, J. Murthy, C. Prakash, S. P. Vanka, Pressure-based finite-volume methods in computational fluid dynamics, Journal of Heat Transfer 129 (4) (2007) 407–424.
URL https://doi.org/10.1115/1.2716419

[8] S. T. Bose, G. I. Park, Wall-modeled large-eddy simulation for complex turbulent flows, Annual review of fluid mechanics 50 (2018) 535–561.

[9] U. Piomelli, E. Balaras, Wall-layer models for large-eddy simulations, Annual review of fluid mechanics 34 (1) (2002) 349–374.

[10] B. Launder, D. B. Spalding, The numerical computation of turbulent flows, Computer Methods in Applied Mechanics and Engineering 3 (2) (1974) 269 – 289.
URL https://doi.org/10.1016/0045-7825(74)90029-2

[11] J. Bredberg, On the wall boundary condition for turbulence models, Chalmers University of Technology, Department of Thermo and Fluid Dynamics. Internal Report 00/4.

[12] W. M. Kays, Turbulent Prandtl NumberWhere Are We?, Journal of Heat Transfer 116 (2) (1994) 284–295.
URL https://doi.org/10.1115/1.2911398

[13] O. Cabrit, F. Nicoud, Direct simulations for wall modeling of multicomponent reacting compressible turbulent flows, Physics of Fluids 21 (5) (2009) 055108.
URL https://doi.org/10.1063/1.3123528

[14] W. M. Kays, Convective heat and mass transfer, Tata McGraw-Hill Education, 2012.

[15] C. Angelberger, T. Poinsot, B. Delhay, Improving near-wall combustion and wall heat transfer modeling in si engine computations, Tech. rep., SAE Technical Paper (1997).

[16] Z. Han, R. D. Reitz, A temperature wall function formulation for variable-density turbulent flows with application to engine convective heat transfer modeling, International journal of heat and mass transfer 40 (3) (1997) 613–625.

[17] F. Berni, G. Cicalese, S. Fontanesi, A modified thermal wall function for the estimation of gas-to-wall heat fluxes in CFD in-cylinder simulations of high performance spark-ignition engines, Applied Thermal Engineering 115 (2017) 1045–1062.

[18] C. Rakopoulos, G. Kosmadakis, E. Pariotis, Critical evaluation of current heat transfer models used in CFD in-cylinder engine simulations and establishment of a comprehensive wall-function formulation, Applied Energy 87 (2010) 1612–1630.
URL https://doi.org/10.1016/j.apenergy.2009.09.029

[19] K. Y. Huh, I.-P. Chang, J. K. Martin, A comparison of boundary layer treatments for heat transfer in ic engines, in: International Congress & Exposition, SAE International, 1990.
URL https://doi.org/10.4271/900252

[20] R. D. Reitz, Assessment of wall heat transfer models for premixed-charge engine combustion computations, in: International Congress & Exposition, SAE International, 1991.
URL https://doi.org/10.4271/910267

[21] D. O. Nijeweme, J. Kok, C. Stone, L. Wyszynski, Unsteady in-cylinder heat transfer in a spark ignition engine: experiments and modelling, Proceedings of the Institution of Mechanical Engineers, Part D: Journal of Automobile Engineering 215 (6) (2001) 747–760.

[22] R. H. Nichols, C. C. Nelson, Wall function boundary conditions including heat transfer and compressibility, AIAA Journal 42 (6) (2004) 1107–1114.
URL https://doi.org/10.2514/1.3539

[23] F. White, G. Christoph, A simple new analysis of compressible turbulent two-dimensional skin friction under arbitrary conditions, Tech. rep. (1971).

[24] L. Back, P. Massier, H. Gier, Convective heat transfer in a convergent-divergent nozzle, International Journal of Heat and Mass Transfer 7 (5) (1964) 549–568.

[25] V. Fico, L. Cutrone, F. Battista, Assessment of wall-functions $k - \epsilon$ turbulence models for the prediction of the wall heat flux in rocket combustion chambers, in: 44th AIAA/ASME/SAE/ASEE Joint Propulsion Conference & Exhibit, 2008, p. 4558.

[26] D. Muto, Y. Daimon, T. Shimizu, H. Negishi, An equilibrium wall model for reacting turbulent flows with heat transfer, International Journal of Heat and Mass Transfer 141 (2019) 1187–1195.

[27] C. M. Palma, S. Silvestri, G. Schlieben, C. Kirchberger, O. Haidn, O. Knab., Injector characterization for a gaseous oxygen-methane single element combustion chamber, Progress in Propulsion Physics 8 (2016) 145–164.

[28] S. Silvestri, M. P. Celano, G. Schlieben, O. Haidn., Characterization of a multi-injector GOx-GCH4 combustion chamber, 52nd AIAA/SAE/ASEE Paper.

[29] N. Perakis, O. J. Haidn, Inverse heat transfer method applied to capacitively cooled rocket thrust chambers, International Journal of Heat and Mass Transfer 131 (2019) 150–166.

[30] A. Chemnitz, T. Sattelmayer, C. Roth, O. Haidn, Y. Daimon, R. Keller, P. Gerlinger, J. Zips, M. Pfitzner, Numerical investigation of reacting flow in a methane rocket combustor: Turbulence modeling, Journal of Propulsion and Power 34 (4) (2017) 864–877.

[31] J. Zips, C. Traxinger, M. Pfitzner, Time-resolved flow field and thermal loads in a single-element gox/gch4 rocket combustor, International Journal of Heat and Mass Transfer 143 (2019) 118474.

[32] J. Zips, C. Traxinger, P. Breda, M. Pfitzner, Assessment of presumed/transported probability density function methods for rocket combustion simulations, Journal of Propulsion and Power 35 (4) (2019) 747–

764.

URL `https://doi.org/10.2514/1.B37331`

[33] D. Maestro, B. Cuenot, L. Selle, Large eddy simulation of flow and combustion in a single-element gch4/gox rocket combustor, in: 7th European Conference for Aeronautics and Space Sciences (EUCASS), 2017.

[34] P. Breda, M. Pfitzner, N. Perakis, O. Haidn, Generation of non-adiabatic flamelet manifolds: comparison of two approaches applied on a single-element GCH4/GO2 combustion chamber, in: 8th European Conference for Aeronautics and Space Sciences (EUCASS), 2019.

[35] N. Perakis, O. J. Haidn, D. Eiringhaus, D. Rahn, S. Zhang, Y. Daimon, S. Karl, T. Horchler, Qualitative and Quantitative Comparison of RANS Simulation Results for a 7-Element GOX/GCH4 Rocket Combustor.
URL `https://arc.aiaa.org/doi/abs/10.2514/6.2018-4556`

[36] P. E. Lapenna, P. P. Ciottoli, F. Creta, Unsteady non-premixed methane/oxygen flame structures at supercritical pressures, Combustion Science and Technology 189 (12) (2017) 2056–2082.

[37] N. Peters, Laminar diffusion flamelet models in non-premixed turbulent combustion, Progress in energy and combustion science 10 (3) (1984) 319–339.

[38] B. Betti, D. Bianchi, F. Nasuti, E. Martelli, Chemical reaction effects on heat loads of CH4/O2 and H2/O2 rockets, AIAA Journal 54 (1) (2016) 1693–1703.

[39] D. Rahn, H. Riedmann, O. Haidn, Extension of a non-adiabatic flamelet combustion model for composition predictions in thermal boundary layers, in: 8th European Conference for Aeronautics and Space Sciences (EUCASS), 2019.

[40] J. Zips, H. Müller, M. Pfitzner, Non-adiabatic tabulation methods to predict wall-heat loads in rocket combustion, in: 55th AIAA Aerospace Sciences Meeting, 2017, p. 1469.

[41] J. Wei, M. Ye, S. Zhang, J. Qin, O. J. Haidn, Modeling of a 7-elements GOX/GCH4 combustion chamber using RANS with Eddy-Dissipation Concept model, Aerospace Science and Technology 99 (2020) 105762.

[42] B. Marracino, D. Lentini, Radiation modelling in non-luminous non-premixed turbulent flames, Combustion Science and Technology 128 (1997) 23–48.

[43] P. E. Lapenna, G. Indelicato, R. Amaduzzi, D. Durigon, R. Lamioni, F. Creta, Consistent flamelet-based turbulent combustion modeling for liquid rocket engines, in: Joint meeting the german and italian sections of the combustion institute, 2018.

[44] P. E. Lapenna, R. Amaduzzi, D. Durigon, G. Indelicato, F. Nasuti, F. Creta, Simulation of a single-element GCH4/GOx rocket combustor using a non-adiabatic flamelet method, in: 2018 Joint Propulsion Conference, 2018, p. 4872.

[45] S.-K. Kim, M. Joh, H. S. Choi, T. S. Park, Multidisciplinary simulation of a regeneratively cooled thrust chamber of liquid rocket engine: Tur-

bulent combustion and nozzle flow, International Journal of Heat and Mass Transfer 70 (2014) 1066–1077.

[46] D. Lee, S. Thakur, J. Wright, M. Ihme, W. Shyy, Characterization of flow field structure and species composition in a shear coaxial rocket GH2/GO2 injector: Modeling of wall heat losses, 47th AIAA/ASME/SAE/ASEE Joint Propulsion Conference and Exhibit 2011.
URL https://doi.org/10.2514/6.2011-6125

[47] P. Wollny, B. Rogg, A. Kempf, Modelling heat loss effects in high temperature oxy-fuel flames with an efficient and robust non-premixed flamelet approach, Fuel 216 (2018) 44 – 52.
URL https://doi.org/10.1016/j.fuel.2017.11.127

[48] P. C. Ma, H. Wu, M. Ihme, J.-P. Hickey, Nonadiabatic flamelet formulation for predicting wall heat transfer in rocket engines, AIAA Journal 56 (6) (2018) 2336–2349.

[49] A. Cuoci, A. Frassoldati, T. Faravelli, E. Ranzi, Opensmoke++: An object-oriented framework for the numerical modeling of reactive systems with detailed kinetic mechanisms, Computer Physics Communications 192 (2015) 237–264.

[50] P. E. Lapenna, G. Indelicato, R. Lamioni, F. Creta, Modeling the equations of state using a flamelet approach in lre-like conditions, Acta Astronautica 158 (2019) 460–469.

[51] G. P. Smith, D. M. Golden, M. Frenklach, N. W. Moriarty, B. Eiteneer, M. Goldenberg, C. Bowman, R. Hanson, S. Song, W. G. et al., Gri-mech 3.0, 2000 URL http://www. me. berkeley. edu/gri. mech.

[52] T. Kim, Y. Kim, S.-K. Kim, Effects of pressure and inlet temperature on coaxial gaseous methane/liquid oxygen turbulent jet flame under transcritical conditions, The Journal of Supercritical Fluids 81 (2013) 164–174.

[53] G. Indelicato, F. Vona, A. Remiddi, P. E. Lapenna, F. Creta, A flamelet-based numerical framework for the simulation of low-to-high mach number flows in LRE, in: AIAA Propulsion and Energy 2020 Forum, 2020, p. 3822.
URL https://doi.org/10.2514/6.2020-3822

[54] P. E. Lapenna, P. P. Ciottoli, F. Creta, The effect of fuel composition on the non-premixed flame structure of LNG/LOx mixtures at supercritical pressure, in: 54th AIAA Aerospace Sciences Meeting, 2016, p. 0690.

[55] S. S. Girimaji, Assumed β-pdf model for turbulent mixing: Validation and extension to multiple scalar mixing, Combustion Science and Technology 78 (4-6) (1991) 177–196.
URL https://doi.org/10.1080/00102209108951748

[56] S. S. Girimaji, Modeling turbulent scalar mixing as enhanced diffusion, Combustion Science and Technology 97 (1-3) (1994) 85–98.
URL https://doi.org/10.1080/00102209408935369

[57] P. E. Lapenna, F. Creta, Direct numerical simulation of transcritical jets at moderate reynolds number, AIAA Journal 57 (6) (2019) 2254–2263.

[58] P. E. Lapenna, F. Creta, Mixing under transcritical conditions: An a-priori study using direct numerical simulation, The Journal of Supercritical Fluids 128 (2017) 263–278.

[59] E. R. Van Driest, Turbulent boundary layer in compressible fluids, Journal of the Aeronautical Sciences 18 (3) (1951) 145–160.
URL https://doi.org/10.2514/8.1895

[60] A. Trettel, J. Larsson, Mean velocity scaling for compressible wall turbulence with heat transfer, Physics of Fluids 28 (2) (2016) 026102.
URL https://doi.org/10.1063/1.4942022

[61] F. Moukalled, L. Mangani, M. Darwish, Turbulence Modeling, Springer International Publishing, Cham, 2016, pp. 693–744.
URL https://doi.org/10.1007/978-3-319-16874-6$_1$7

[62] B. Launder, D. Spalding, The numerical computation of turbulent flows, Computer Methods in Applied Mechanics and Engineering 3 (2) (1974) 269 – 289.

[63] D. C. Wilcox, et al., Turbulence modeling for CFD, Vol. 2, DCW industries La Canada, CA, 1998.

[64] P. C. Ma, X. I. A. Yang, M. Ihme, Structure of wall-bounded flows at transcritical conditions, Phys. Rev. Fluids 3 (2018) 034609.
URL https://link.aps.org/doi/10.1103/PhysRevFluids.3.034609

[65] L. Davidson, B. Farhanieh, Report 95/11, Dept. of Thermo and Fluid Dynamics, Chalmers University of Technology, Gothenburg.

[66] J. Yang, J. Martin, Approximate solutio one-dimensional energy equation for transient, compressible, low mach number turbulent boundary layer flows, Journal of Heat Transfer 111 (3) (1989) 619–624.
URL https://doi.org/10.1115/1.3250727

[67] K. Y. Huh, I.-P. Chang, J. K. Martin, A comparison of boundary layer treatments for heat transfer in ic engines, 1990.

[68] W. C. Reynolds, Computation of turbulent flows, Annual Review of Fluid Mechanics 8 (1) (1976) 183–208.

[69] M. Ikegami, Y. Kidoguchi, K. Nishiwaki, A multidimensional model prediction of heat transfer in non-fired engines, Tech. rep., SAE Technical Paper (1986).

[70] H. Jasak, A. Jemcov, Z. Tukovic, et al., Openfoam: A C++ library for complex physics simulations, in: International workshop on coupled methods in numerical dynamics, Vol. 1000, IUC Dubrovnik Croatia, 2007, pp. 1–20.

[71] G. Indelicato, P. E. Lapenna, D. Durigon, F. Creta, Simulations of turbulent combustion and wall heat transfer in single and multi injectors GCH4/GOX rocket combustors, in: 8th European Conference for Aeronautics and Space Sciences (EUCASS), 2019.

[72] G. Indelicato, P. E. Lapenna, R. Concetti, M. Caputo, M. Valorani,

G. Magnotti, F. Creta, Numerical investigation of high pressure CO2-diluted combustion using a flamelet-based approach, Combustion Science and Technology (2020) 1–22.

[73] J. H. Ferziger, M. Peric, Computational methods for fluid dynamics, Springer Science Business Media, 2012.

[74] R. P. Brent, Algorithms for minimization without derivatives, Courier Corporation, 2013.

[75] B. E. Launder, B. Sharma, Application of the energy-dissipation model of turbulence to the calculation of flow near a spinning disc, Letters in heat and mass transfer 1 (2) (1974) 131–137.

[76] F. Winter, S. Silvestri, M. P. Celano, G. Schlieben, O. Haidn, High-speed and emission imaging of a coaxial single element GOX/GCH4 rocket combustion chamber, in: European Conference for Aeronautics and Space Sciences, 2017.

[77] T. Fiala, T. Sattelmayer, Assessment of existing and new modeling strategies for the simulation of OH* radiation in high-temperature flames, CEAS Space Journal 8 (1) (2016) 47–58.

[78] J.-P. Legier, T. Poinsot, D. Veynante, Dynamically thickened flame les model for premixed and non-premixed turbulent combustion, in: Proceedings of the summer program, Vol. 12, Center for Turbulence Research Stanford, CA, 2000.

[79] F. Nicoud, F. Ducros, Subgrid-scale stress modelling based on the square

of the velocity gradient tensor, Flow, turbulence and Combustion 62 (3) (1999) 183–200.